# RF-Behavior: A Multimodal Radio-Frequency Dataset for Human Behavior and Emotion Analysis

SI ZUO, Aalto University, Finland YUQING SONG, Aalto University, Finland SAHAR GOLIPOOR, Aalto University, Finland YING LIU\*, Aalto University, Finland XUJUN MA, Télécom SudParis, France STEPHAN SIGG, Aalto University, Finland

Recent research has demonstrated the complementary nature of camera-based and inertial data for modeling human gestures, activities, and sentiment. Yet, despite its growing importance for environmental sensing as well as the advance of joint communication and sensing for prospective WiFi and 6G standards, a dataset that integrates these modalities with radio frequency data (radar and RFID) remains rare. We introduce *RF-Behavior*, a multimodal radio frequency dataset for comprehensive human behavior and emotion analysis. We collected data from 44 participants performing 21 gestures, 10 activities, and 6 sentiment expressions. Data were captured using synchronized sensors, including 13 radars (8 ground-mounted and 5 ceiling-mounted), 6 to 8 RFID tags (attached to each arm) and LoRa. Inertial measurement units (IMUs) and 24 infrared cameras are used to provide precise motion ground truth. RF-Behavior provides a unified multimodal dataset spanning the full spectrum of human behavior – from brief gestures to activities and emotional states – enabling research on multi-task learning across motion and emotion recognition. Benchmark results demonstrate that the strategic sensor placement is complementary across modalities, with distinct performance characteristics across different behavioral categories.

 $\hbox{CCS Concepts:} \bullet \textbf{Human-centered computing} \to \textbf{Ubiquitous and mobile computing design and evaluation methods}.$ 

Additional Key Words and Phrases: RF sensing, gesture recognition, human activity recognition, sentiment analysis

## 1 Introduction

Human-computer interaction, ambient intelligence, and ubiquitous computing depend on robust perception of hand gestures, daily activity, and human sentiment. While numerous datasets exist for gesture recognition, human activity recognition and emotion analysis, most of them rely on a single behavioral dimension (e.g., gestures or activities) and a narrow sensing modality, which limits generalization to real environments and hinders cross-task transfer. To bridge these gap, we introduce a new multimodal dataset that jointly captures hand gestures, full-body activities and sentiment state using heterogeneous sensors: Depending on the measurement campaign, up to 13 millimeter-wave radars (8 ground-mounted and 5 ceiling-mounted) providing multi-angle RF views, 6 to 8 RFID tags, LoRa, body-worn IMUs, and time-series motion data from up to 24 infrared cameras. Data were collected from 44 participants, each performing 21 hand gestures, 10 activities and 6 sentiment states, enabling research in multimodal fusion and robust recognition across viewpoints.

Existing gesture recognition datesets have made significant contributions to the field. The DVS128 Gesture dataset [2] provides event-based cameras for gesture recognition. It contains 11 hand gestures from 29 subjects under 3 illumination conditions. The dataset offers temporal precision but lacking the rich multimodal context. The SHREC dataset [13] focuses on hand gesture recognition using depth cameras, providing detailed hand tracking. These vision-centric approaches, while valuable, face privacy concerns and a degradation on performance when

Authors' Contact Information: Si Zuo, Aalto University, Espoo, Finland, si.zuo@aalto.fi; Yuqing Song, Aalto University, Espoo, Finland, yuqing.song@aalto.fi; Sahar Golipoor, Aalto University, Espoo, Finland, sahar.golipoor@aalto.fi; Ying Liu, Aalto University, Espoo, Finland, ying.2.liu@aalto.fi; Xujun Ma, Télécom SudParis, Palaiseau, France, xujun.ma@telecom-sudparis.eu; Stephan Sigg, Aalto University, Espoo, Finland, stephan.sigg@aalto.fi.

<sup>\*</sup>Corresponding author

the environmental conditions are not ideal (e.g., poor lighting and occlusion). Instead of collecting vision data, the Pantomime dataset [34] includes 21 gestures from 8 millimeter-wave radars placed on the ground.

Activity recognition datasets emphasize on-body IMU or RGB without ambient RF information. The UCI HAR dataset [3] utilizes accelerometer and gyroscope data from a smartphone for activity recognition. It demonstrates the potential of wearable sensors but limits the recognition to body-worn devices. The similar condition also apply to WISDM [26] and PMAMP2 [36] datasets. The OPPORTUNITY dataset [38] introduces a more comprehensive approach with multiple body-worn sensors for activities of daily living. Video-based datasets like Kinetics [22] and ActivityNet [9] provide rich visual information for activity but inherit the computational costs, privacy concerns, and environmental sensitivity due to the camera-based systems.

Sentiment and emotion analysis datasets predominantly rely on facial expressions, speech and physiological signals. Emotion datasets such as DEAP [25] (EEG/physiology and video) and AffectNet [32] (facial images) focuses on sentiment states but omits the motion information (gestures/activities). Speech-based datasets like IEMOCAP [8] provide rich emotional cues but fail in noisy environments or when subjects are silent. While some multimodal emotion datasets exist, such as RECOLA [37], they typically combine audio-visual modalities that still depend on cameras and microphones, leaving gaps in privacy-preserving, non-intrusive emotion sensing scenarios.

In this paper, we present the comprehensive multimodal dataset *RF-Behavior*, that integrates eight ground-mounted radars, five ceiling-mounted radars, RFID tags, a Lora, inertial measurement units (IMUs), and infrared cameras to capture human behavior across three distinct temporal and complexity scales: 21 hand gestures, 10 activities, and 6 sentiment expressions from 44 participants. To summarize, our contributions are:

- (1) A unified behavioral dataset that covers gestures, activities and sentiment, enabling research on multi-task learning across motion and emotion.
- (2) Complementary sensing with multi-angle RF: thirteen synchronized radars (8 ground, 5 ceiling) provide dense angular diversity. Ceiling-mounted radars offer a potential path toward angle-invariant motion recognition.
- (3) The multi-sensor setup simulates realistic indoor spaces. At the same time, a consistent protocol across 44 participants ensures repeatability, balanced class coverage, and statistically meaningful evaluation across tasks.
- (4) By emphasizing non-visual sensors as primary modalities, our dataset enables behavior recognition without capturing identifiable facial features or RGB imagery, addressing growing privacy concerns in ubiquitous sensing applications.

# 2 Ethical Approval

For the data collection campaigns we have acquired ethical approval by the ethical committee of our institution. Subjects were provided with three documents: A consent form to be signed by the subjects, an information sheet that provides a general description of the research as well as a privacy notice for the data collection. The privacy notice explains in detail how personal data will be used, how we store the data and which rights the participants have according to the GDPR. Thus, for the entire data collection, we ensured that all participants joined voluntarily and were well informed about the collection procedures and the rights they have. To recruit participants, we sent the advertising poster via email lists and put up paper posters on each building at our institution.

Table 1. Comparison of existing gesture, activity, and sentiment recognition datasets with RF-Behavior

Dataset	Type	Modalities	Subjects	Classes	Privacy	Year		
Gesture Recognition Datasets								
NTU RGB+D [43]	Gesture/Activity	RGB, Depth, Skeleton	40	60	Low	2016		
DVS128 [2]	Gesture	Event Camera	29	11	Medium	2017		
SHREC'17 [13]	Hand Gesture	Depth, Skeleton	28	14	Medium	2017		
Soli [29]	Hand Gesture	Radar	10	11	High	2016		
Pantomime [34]	Hand Gesture	Radar	10	21	High	2021		
mHomeGes [30]	Arm Gesture	Radar	25	10	High	2020		
Traffic gesture dataset [23]	Hand Gesture	Radar	35	8	High	2023		
UWB-Gestures [1]	Hand Gesture	Radar	8	12	High	2021		
8-radar dataset [40]	Hand Gesture	Radar	15	21	High	2024		
		Activity Recognition Datasets						
Opportunity [38]	Activity	Multi-sensor (body-worn)	4	21	High	2010		
WISDM [26]	Activity	Accelerometer, Gyroscope	51	18	High	2011		
UCI HAR [3]	Activity	Accelerometer, Gyroscope	30	6	High	2013		
ActivityNet [32]	Activity	RGB Video	N/A	200	Low	2015		
UTD-MHAD [12]	Activity	RGB, Depth, Inertial	8	27	Medium	2015		
Kinetics [22]	Activity	RGB Video	400+	700	Low	2017		
RadHAR [44]	Activity	Radar	2	5	High	2019		
ETRI-Activity3D [20]	Activity	RGB, Depth, Accel	100	55	Medium	2020		
RecGym [4]	Activity	Accelerometer, Gyroscope	10	12	High	2022		
WEAR [5]	Activity	Accelerometer, RGB video	22	18	Medium	2024		
		Sentiment/Emotion Recognition Datasets			•			
IEMOCAP [8]	Emotion	Audio, Video, Motion	10	10	Low	2008		
RECOLA [37]	Emotion	Audio, Video, Physio	46	Continuous	Low	2013		
AffectNet [32]	Emotion	RGB Images	440K	8	Low	2017		
RAF-DB [28]	Emotion	RGB Images	30K	7	Low	2017		
AFFEC [42]	Emotion	EEG, Eye Tracking, GSR,	71	6	Low	2025		
AFTEC [44]	Emotion	Body temperature, Video, Personality	/1	U	LOW	2023		
RF-Behavior	All	Radar, RFID, LoRa, IMU, IR	46	37 (21+10+6)	High	2025		

# Related work

# Gesture Recognition

Gesture recognition has been extensively studied across multiple sensing modalities, including vision, inertial, and radio frequency (RF). Vision-based datasets, such as Chalearn [18] and HaGRID [21], provide large-scale RGB or RGB-D recordings for hand and body gesture understanding. However, these datasets often raise privacy concerns because they require that a human is captured by the camera and used to train the system and are highly sensitive to illumination and occlusion. To overcome these limitations, recent work has focused on radar, RFID and inertial-based gesture recognition. In particular, radar enables contactless sensing and preserves privacy while maintaining robustness under diverse environmental conditions (in contrast to WiFi/CSI-based systems).

Millimeter-wave (mmWave) radar has emerged as a sensing modality for human perception due to its ability to capture fine-grained micro-Doppler or point cloud data. Datasets such as the TI Radar Gesture Dataset mHomeGes [30] and a traffic gesture dataset [23] provide radar-based gesture samples under controlled settings, typically using a single radar device. Shahzad et al. [1] present UWB-Gestures, a pioneering public dataset that captures twelve dynamic hand gestures via ultra-wideband impulse radar sensing. It consists of 9,600 gesture instances acquired from eight volunteers. A dataset comprising more than half a million gesture instances was introduced by Hayashi et al. [19], leveraging Soli radar to support research on improving gesture recognition robustness and generalization. While these datasets have enabled research on radar-based motion recognition, they often contain sparse point clouds, limited spatial coverage, and lack multi-sensor synchronization. Recent studies have attempted to merge data from multiple radars to improve spatial density and field of view [40], yet no dataset provides accurately synchronized, multi-radar, multi-modal measurements with coordinate alignment. RF-Behavior addresses this gap by integrating data from 13 mmWave radars, applying time synchronization and coordinate transformation to produce a unified, denser, and information-rich 3D representation of human motion. 5 radars are fixed on the ceiling, while the remaining radars are placed on the ground surrounding the subject. They provide diverse data from all directions. In addition, researchers can freely choose data from desired radar channels to fit different experimental setups or tasks.

Body-mounted backscattering tags may als be employed to support the perception of gestures, activities and sentiment. In our work, we specifically integrate COTS RFID-type backscattering tags which are standardized and easy to integrate with limited technical complexity. While RFID tags are traditionally associated with identification purposes, studies have also demonstrated their capability for sensing applications [16, 17, 27]. In this regard, few open-source RFID datasets for sensing scenarios are available. In [45], RFID tags were installed on floor mats across the living spaces, and antennas were mounted above the ceiling to monitor human daily activities. For the purpose of tracking assets and optimizing inventory management in retail and industrial environments, data related to RFID tag movement detection have been collected [7]. Unlike the aforementioned studies, where RFID tags are installed in the environment, we embedded RFID tags on different parts of human subjects' arms across multiple campaigns, covering gesture and activity recognition as well as sentiment monitoring. This setup mimicks situations in which the tags are integrated into clotzing, e.g. to allow conscious opt-in to the sensing system. In [6], a different technology, Ultra-Wideband (UWB) transceiver active tags attached to participants, was used alongside other modalities, including WiFi, radar, and vision/infrared, for human activity recognition and localization. In contrast to the above dataset, we used passive RFID tags, which offer the advantages of requiring no manual maintenance and being easy to attach.

# 3.2 Human activity recognition

Human activity recognition (HAR) has evolved significantly over the past decades, progressing from simple accelerometer-based classification to complex multimodal sensing systems. Early HAR research primarily relied on wearable inertial sensors, with pioneering datasets such as WISDM [26] utilizing smartphone accelerometers to recognize six basic activities. The UCI HAR dataset [3] expanded this approach by incorporating both accelerometer and gyroscope data from 30 subjects, establishing a widely-used benchmark for wearable sensor-based activity recognition. These wearable-centric approaches demonstrated the feasibility of continuous activity monitoring but faced practical limitations including user compliance, battery life constraints, and the requirement for subjects to consistently carry or wear devices.

To address the limitations of on-body sensing, researchers have explored ambient and contact-free sensing modalities. The Opportunity dataset [38] introduced a comprehensive approach with 72 sensors distributed across the body and environment to capture activities of daily living, demonstrating the potential of dense sensor networks but highlighting deployment complexity. PAMAP2 [36] incorporated physiological signals alongside inertial measurements, collecting data from 9 subjects performing 18 activities with multiple IMUs and heart rate monitors placed at different body locations.

Vision-based approaches have gained prominence with the advent of affordable depth cameras and advances in computer vision. The NTU RGB+D dataset [43] provided large-scale RGB and depth video data with 3D skeletal joint annotations for 60 action classes performed by 40 subjects, becoming one of the most widely-used benchmarks for skeleton-based action recognition. Large-scale video datasets such as Kinetics [22] and ActivityNet [32] enabled deep learning approaches for activity recognition in unconstrained environments, with hundreds of activity categories captured from diverse real-world scenarios. However, vision-based systems face

fundamental challenges including sensitivity to lighting conditions, occlusions, computational demands, and privacy concerns that limit their deployment in sensitive environments such as homes and healthcare facilities.

Radio frequency (RF) sensing has emerged as a compelling alternative that addresses many limitations of traditional approaches. WiFi-based sensing techniques [46] demonstrated that channel state information (CSI) can be leveraged for device-free activity recognition by analyzing wireless signal perturbations caused by human movement. Radar-based sensing offers particular advantages for privacy-preserving HAR, with millimeter-wave radar systems operating in the 60-81 GHz range providing fine-grained motion detection without capturing identifiable visual information [24]. The Soli dataset [29] introduced 60 GHz radar for hand gesture recognition, demonstrating high accuracy for 11 gesture classes but focusing exclusively on fine-grained hand movements. Recent radar-based datasets such as RadHAR [44] extended this to full-body activity recognition using FMCW (Frequency Modulated Continuous Wave) radar, though typically with limited activity categories and singleviewpoint sensing. It contains sparse point clouds from a low-cost mmWave radar, aggregated over time into voxel representations for classifying five human activities.

#### 3.3 Sentiment analysis

Sentiment and emotion recognition has been extensively studied across multiple modalities, including facial expressions, speech signals, physiological measurements and text analysis. Early emotion recognition research focused primarily on facial expressions, building upon Ekman's theory of universal emotions [15]. Large-scale facial emotion datasets have enabled significant advances in this domain. AffectNet [32] compiled over 440,000 facial images with annotations for eight discrete emotion categories and continuous valence-arousal values. RAF-DB [28] provided 30,000 real-world facial images with basic and compound emotion annotations. These datasets require clear facial visibility and raise substantial privacy concerns, limiting their applicability in privacy-sensitive contexts.

Multimodal emotion recognition approaches have demonstrated that combining multiple signal sources can improve recognition accuracy and robustness. IEMOCAP [8] provided a landmark multimodal dataset with audio, video, and motion capture data from 10 actors performing scripted and improvised emotional scenarios. RECOLA [37] addressed the limitation of controlled scripted acting in IEMOCAP by capturing spontaneous emotion behavior during collaborative tasks from 46 participants.

Physiological signal-based emotion recognition has explored the relationship between internal body states and emotional experiences. The DEAP dataset [25] collected EEG and peripheral physiological signals while participants watched music videos designed to provoke specific emotions. The WESAD dataset [41] focused on stress and affect detection using wearable sensors measuring electrodermal activity, blood volume pulse, respiration, and temperature during controlled stress induction protocols.

Recent research has explored contact-free approaches for emotion recognition to address privacy and comfort concerns. Thermal imaging has been investigated for stress and emotion detection through facial temperature patterns [33], offering privacy advantages over RGB cameras while capturing physiological manifestations of emotional states. RF-based sensing has shown potential for emotion recognition through analysis of subtle physiological signals such as respiration and heart rate patterns captured via radar [31]. Text-based emotion analysis has achieved remarkable success using transformer-based language models [14], but focuses on expressed opinions rather than experienced emotional states.

A critical limitation of existing emotion datasets is their focus on brief, discrete emotional moments rather than long-lasting emotions. Most datasets capture emotions lasting seconds to a few minutes, often in response to controlled stimuli, failing to represent the temporal dynamics of real emotional experiences. Additionally, most of the public emotion datasets rely on either facial video, which compromises privacy, or scripted emotional displays, which may not reflect authentic affective expressions. The integration of privacy-preserving RF sensing



Fig. 1. The digital studio for data collection.

modalities to continuously capture emotion remains largely unexplored, representing a large gap for real-world deployment in homes, workplaces, and healthcare settings.

## 4 The RF-Behavior Dataset

The RF-Behavior dataset comprises the recognition of 21 gestures, 10 activities and 6 sentiment types, which have been collected from a total of 44 subjects. The collection of the data spanned two months with 30 individual recording campaigns and spanning 5 different settings in multiple locations. We split the data collection into four Campaign: Campaigns 1 and 4 on gestures in various locations, Campaign 2 on human activities, Campaign 3 on sentiment. Campaigns 1–3 were conducted in a digital studio (see Fig. 1), while campaign 4 was held at an industrial workplace. The dataset contains simultaneous data from multiple sensors, including Radio-Frequency (RF) data from radars, Radio-Frequency Identification (RFID), LoRa, as well as motion data from three IMU (Inertial Measurement Unit) sensors, along with 24 infrared cameras capturing motion information. The data from the IMUs and infrared cameras serve as the ground truth. The radar operates in the frequency range of 77-81 GHz, RFID works at a frequency of 865 MHz and LoRa at a frequency of 915 MHz.

## 4.1 Sensors

4.1.1 Radar. Thirteen mmWave Frequency-modulated Continuous Wave (FMCW) radars (TI IWR1443) are employed. The radar operates over a 4 GHz bandwidth from 77 GHz to 81 GHz. These radars emit linearly frequency-modulated chirps and determine object range and velocity by comparing the transmitted and reflected signals. The onboard 3 transmit and 4 receive antennas enable object angle estimation. We use FMCW-MIMO technology to generate range-azimuth-elevation maps and convert them into 3D point-cloud data representing reflections from surrounding objects. The resulting point clouds, captured frame by frame in x-y-z coordinates, form spatio-temporal sequences for analysis. When saving the data, the current timestamp, x, y, z, and density are

stored together. Each radar has its own coordinate system, so coordinate transformation and time synchronization are conducted to merge all data.

4.1.2 RFID. We use Alien AZ 9662 passive RFID tags, an Impinj Speedway R420 RFID reader, and a circularly polarized Vulcan RFID PAR90209H antenna with a circular polarization gain of 9 dBiC as well as elevation and azimuth beamwidth of 70°. A laptop running the Impinj ItemTest software is used to control the RFID reader. The RFID system functions at a frequency of 865 MHz with a transmission power of 30 dBm. The tag's integrated circuit (IC) modulates its reply to the reader's continuous wave signal by varying the impedance on its antenna. This change causes the tag to either reflect or absorb portions of the incoming signal, generating reflection coefficient  $\Gamma(t) \in 0$ , 1. The reflection coefficient is  $\Gamma = \frac{Z_{\text{Ant}} - Z_{\text{Load}}(t)}{Z_{\text{Ant}} + Z_{\text{Load}}(t)}$ , where  $Z_{\text{Ant}}$  and  $Z_{\text{Load}}(t)$  denote the antenna impedance (around 50 $\Omega$ ) and the load impedance controlled by the tag's IC. When  $Z_{\text{Load}} = Z_{\text{Ant}}$ , the reflection coefficient becomes  $\Gamma=0$ , meaning no signal is reflected. Conversely, when  $Z_{\text{Load}}=0$ , the reflection coefficient reaches  $\Gamma = 1$ , and the reader's signal is fully reflected. In practice, due to imperfect load matching,  $\Gamma$  typically varies between values that are approximately 0 and 1. We denote the basedband received signal at the reader by

$$y(t) = \sum_{i=1}^{N_p} g_i G_a \sqrt{P_t} s(t) + v(t); \quad y(t) \in \mathbb{C}.$$
 (1)

where  $g_i \triangleq \frac{\lambda}{4\pi d_i} e^{j\theta_i}$  denotes the channel gain of the *i*th round-trip path with  $\theta_i \sim \mathcal{U}[0, 2\pi)$ , wavelength  $\lambda$ , path distance  $d_i$ , the number of multipath components  $N_p$ , antenna gain  $G_a$ , reader transmit power  $P_t$  and the transmitted signal s(t). v(t) represents the additive thermal noise at the reader, modeled as a zero-mean Gaussian random variable with variance  $\sigma^2$ . The data obtained from the tag includes Electronic Product Code (EPC), a timestamp, the Received Signal Strength (RSS), and the signal phase.

4.1.3 LoRa. LoRa employs CSS modulation to achieve long-range communication. A Commercial Semtech SX1276 RF module configured by an Arduino Uno board is utilized as the LoRa node for transmitting LoRa signals via a bipolar antenna. The LoRa node sends a series of linear chirps, each characterized by its duration T and frequency bandwidth B. CSS modulates the data by varying the starting frequency and the slope of the chirp. Fig. 16a illustrates the signal spectrum of a typical LoRa packet. The packet begins with a preamble containing full up-chirps. Subsequently, two down-chirps are transmitted to represent the start frame delimiter (SFD). After the SFD, chirps with different starting frequencies are used to encode the data to be transmitted. The encoded data bits within a chirp are defined by the Spreading Factor (SF). LoRa supports seven different spread factors, ranging from 6 to 12. Each chirp can encode data using 2<sup>SF</sup> different starting frequencies. By default, the LoRa node is configured to transmit signals with a carrier frequency of 865.5 MHz with a bandwidth of 125 kHz. To interpret the LoRa signals, a USRP N200 co-located with the LoGa node is configured as a LoRa gateway to receive the reflected LoRa signals. The received LoRa signals are down-converted to the baseband and then sampled by ADC with 500 kHz sampling rate. The amplitude of the baseband signal is exported for sensing purposes.

IMU. We used three Movesense sensors 1 for IMU data collection. Movesense is a battery-powered device that incorporates low power sensor components with Bluetooth Low Energy (BLE) enabled Micro Controller Unit (MCU). Is based on Nordic Semiconductor's nRF52 BLE chip fitted with 9-axis motion sensor (3-axis accelerometer, 3-axis gyroscope and 3-axis magnetometer). We used the sampling frequency of 52Hz for the gesture collection and 104Hz for the rest of the campaigns. Three *Movesense* sensors were placed on various parts of the human body in different campaigns.

<sup>&</sup>lt;sup>1</sup>https://www.movesense.com/docs/

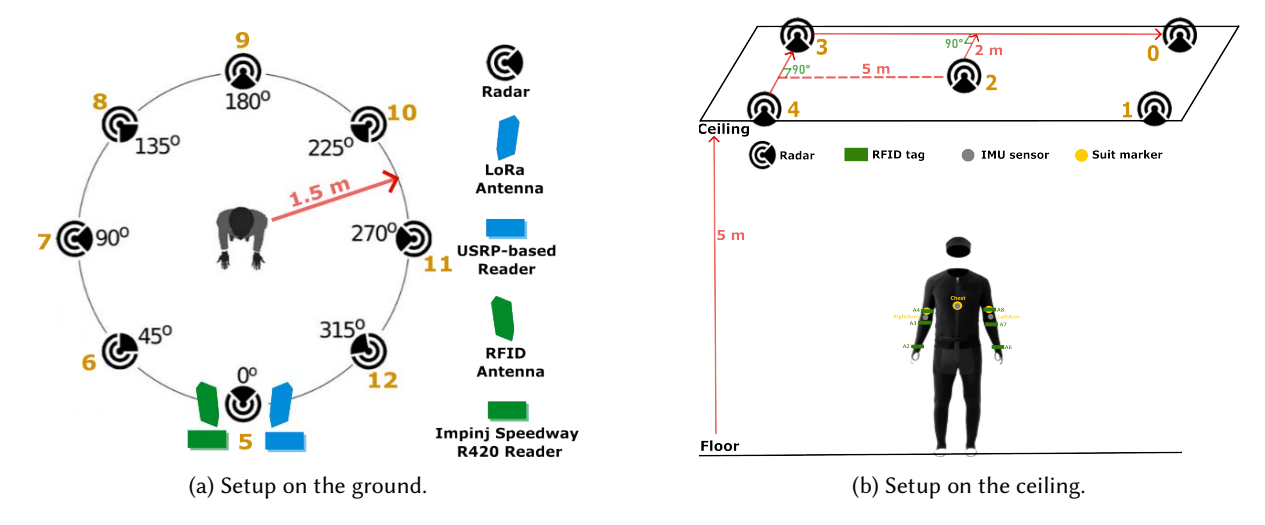


Fig. 2. Setup for Campaign 1: gesture data collection.

4.1.5 Infrared Camera. The digital studio is equipped with 24 infrared cameras for motion tracking. The camera-based system uses multiple synchronized cameras to capture motion from different angles by tracking reflective markers placed on the human body. Cameras are strategically positioned around the studio to cover the entire recording area and to minimize occlusions. Data from all cameras are fused to reconstruct a three-dimensional trajectory for each marker via triangulation, after which the system computes the spatial positions to digitally reconstruct the motion. The sampling rate was set to 100 Hz for all recording campaigns.

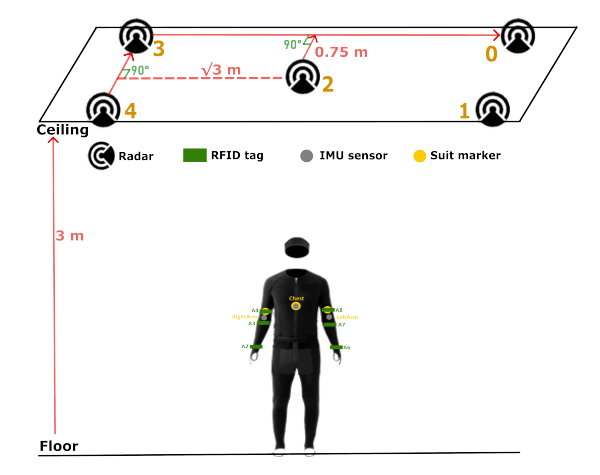
## 4.2 Environmental Setup

4.2.1 Campaigns 1 & 4 (Gestures). Fig. 2 illustrates the environment setup, which comprises two sections: ground and ceiling. The number next to the radar symbol indicates the index of the radar. During each data collection experiment, a subject is positioned on the ground, at the center of a circular configuration with a radius of 1.5 meters. Surrounding the subject, there are eight radars placed at specific angular coordinates: 0°, 45°, 90°, 135°, 180°, 225°, 270°, and 315°. These radars detect movement and velocity by measuring reflected radio waves. At the 0° position, an RFID antenna was installed and connected to an Impinj Speedway R420 reader to receive backscattered signals from passive RFID tags attached to the subject.

On the ceiling, four radars were positioned in each corner, spaced 4 meters apart on one side and 10 meters apart diagonally on the opposite side, providing comprehensive coverage of movement within the area. An additional radar was placed in the center of the ceiling, directly above the subject. Furthermore, 24 infrared cameras were arranged around the space at various angles and heights to ensure unobstructed views as the subject performs gestures from a standing position (see Fig. 4).

After preliminary experiments, we decided to lower the height to 3 meters and reposition the four radars at the corners of the ceiling: 1.5 meters apart on one side and  $2\sqrt{3}$  meters apart diagonally on the opposite side. These adjustments (as illustrated in Fig. 3) were made to improve the detection of hand movements and enhance the overall accuracy of motion information collected.

These sensors are concentrated on the upper part of the human body, as most gestures involve upper-body movements. This strategic placement ensures accurate data collection for gesture recognition, focusing on areas



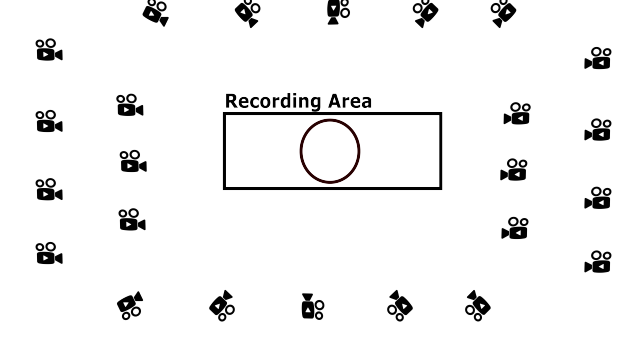


Fig. 3. Ceiling setup adjustment.

Fig. 4. Infrared camera setup for data collection: The circle represents the recording area for gesture data collection, while the rectangle represents the area for human activities and sentiment data collection.

with significant motion activity. As the subject performs gestures, the movement is captured by sensors placed on the body as well as devices positioned on the ground and ceiling.

4.2.2 Campaign 2 (Human activities). For the human activity collection in Campaign 2, we maintained the ceiling setting and modified the experimental setup on the ground by enlarging the recording area to 6m x 2m (see Fig. 5). Radar devices were placed to ensure comprehensive coverage: devices with indices 6, 7, and 8 were aligned along one of the long sides, devices 10, 11, and 12 were on the opposite side, and devices 5 and 9 were centered on the shorter ends. Within this area, the RFID and LoRa antennas were also placed to capture multi-modal data during the activities.

The adjustment of the setup compared to the previous campaign was primarily due to the fundamentally different requirements of the target activities versus gestures, particularly the need for more space. The previous circular setup (1.5-meter radius) was too restrictive for full-body dynamic activities. Motions like walking, running, playing badminton, and kicking a football require significant room for participants to move naturally, and the 6m x 2m rectangular area provides this necessary space. The surrounding radar placement allows for the capture of activities from multiple angles, which is especially beneficial for tasks like walking and running. For these, participants followed an "S"-shaped trajectory (see Fig. 8a and Fig. 8b) that covered the full recording area. This trajectory enabled a longer distance for the movement, resulting in a greater recording length per repetition. The rest of the activities were primarily performed around the center point of the area, which is why the RFID and LoRa antenna are placed directly in front of this central location.

As indicated by the red arrows and text in the figure, the distances between the radar nodes were asymmetrical. Notably, the spacing between radars 8, 7, and 6 is greater than the spacing between radars 10, 11, and 12, which is on purpose. For sports-related activities, participants were instructed to face the side with radars 6, 7, and 8 when throwing a basketball, playing badminton/floorball, or kicking a football. To ensure the safety of the equipment and provide adequate space for these actions, we increased the distance between the devices on that side.

Furthermore, to ensure the highest positional accuracy, we addressed a discrepancy observed between the desired and the actual physical placements of the devices. We precisely localized the exact 3D coordinates of each radar device using an infrared camera system in the studio. For this process, the center (see Fig. 5) of the experimental area was established as the origin point (0, 0, 0). Establishing this unified coordinate system is

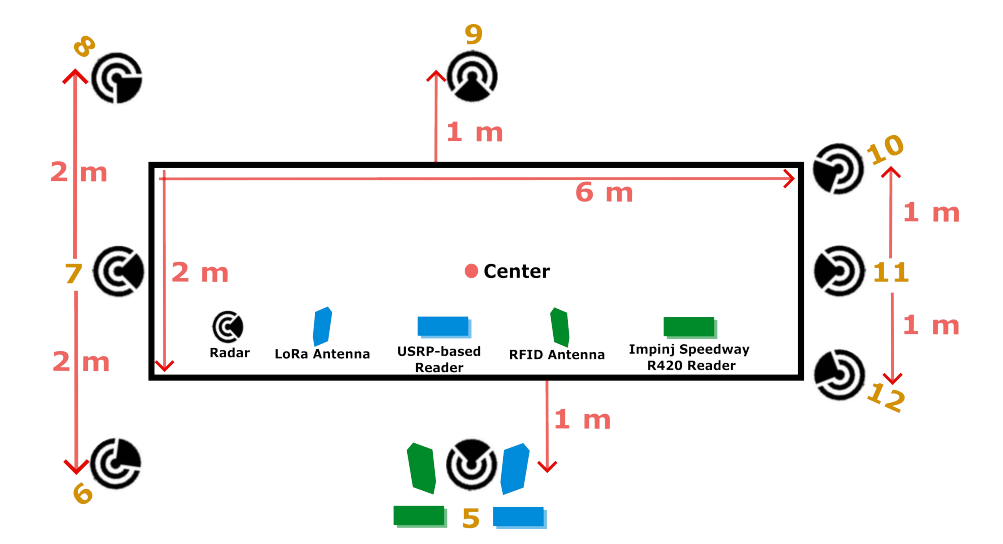


Fig. 5. Setup on the ground for Campaign 2: human activity collection.

Table 2. Measured 3D coordinates of the radar devices based on the ground-truth data from the infrared cameras in the recorded area.

Radar Device	X	Y	Z
Device 5	2.6055	-0.0940	0.9407
Device 6	1.8044	-3.4535	0.8953
Device 7	-0.2786	-3.1746	0.9019
Device 8	-2.6325	-3.0253	0.8815
Device 9	-2.9319	-0.1305	0.8704
Device 10	-1.1499	3.2323	0.8784
Device 11	0.0234	3.1029	0.9253
Device 12	1.1062	2.8954	0.9261

significantly useful for synchronizing data from the different radars. The final coordinates for the eight radar nodes on the ground are listed below:

- 4.2.3 Campaign 3 (Sentiment). The environmental setup for our sentiment data collection was nearly identical to that of the human activity collection, preserving the device settings on the ceiling and around the 6m x 2m rectangular ground area. The sentiment campaign required a specific setup with a desk and chair centered in the recording area. A screen was also placed in front of the participant outside the recording area, as shown in Fig. 6. The sentiment data collection was split into two parts: while the screen was present for both, the desk and chair from the first part were removed for the second.
- 4.2.4 Campaign 4 (Gestures). The same equipment described in Section 4 was employed in an industrial laboratory setting (see Fig. 7), involving a different group of participants (totaling 17) along with one additional RFID tag placed on each side of the wrists for data collection.

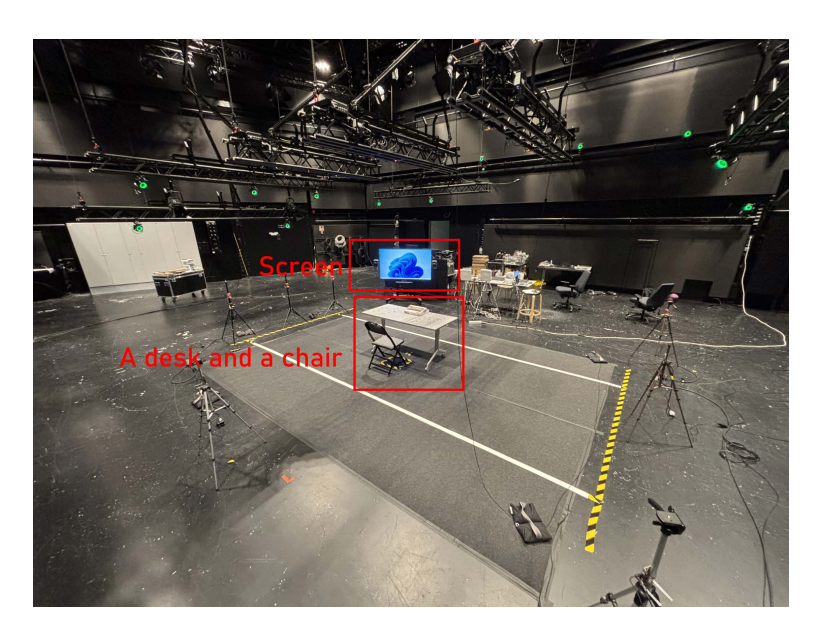


Fig. 6. Ground setup updated for sentiment data collection.

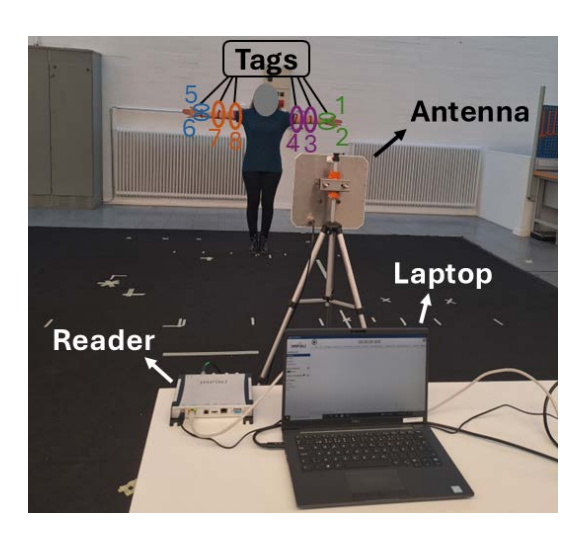


Fig. 7. Experimental setup. Eight passive RFID tags were affixed to the participant. Phase and RSS data were recorded using an Impinj Speedway R420 reader with a circularly polarized antenna as the participants performed gestures at distances of 1.5 m and 3 m from the antenna.

#### **Data Collection & Structure** 4.3

Campaign 1 (Gestures). We collected data from 25 subjects performing 21 gestures, with each gesture repeated 8 times. This gesture set of gestures was originally proposed in [34], and we have utilized the same set but within a different environmental setup. Specifically, here are the names for each gesture: (a) lateral-raise, (b) push-down, (c) lift, (d) pull, (e) push, (f) lateral-to-front, (g) swipe-right, (h) swipe-left, (i) throw (j) arms-swing, (k) two-hand-throw, (l) two-hand-push, (m) two-hand-pull, (n) two-hand-lateral-raise, (o) left-arm-circle, (p) right-arm-circle, (q) two-hand-outward-circles, (r) two-hand-inward-circles, (s) two-hand-ateral-to-front, (t) circle-clockwise, (u) circle-counter-clockwise. The set is divided into two groups, namely easy and complex, according to their execution difficulty. Gestures (a)-(i) are considered to be the easy set, consisting of single-hand motions that are straightforward to execute and recall. The remaining gestures (j)-(u) belong to the complex set, which includes bimanual, linear, and circular movements.

4.3.2 Campaign 2 (Human activities). We collected data from 25 subjects for ten activities (walking, running, sitting, lying, ascending stairs, descending stairs, passing a basketball, playing badminton, playing floorball, and kicking a football; see Fig. 8). Each gesture was repeated 8 times by each subject.

Our selection of activities combines fundamental Activities of Daily Living (ADLs) with more complex sports-related movements. As the most frequent and essential actions in daily life, these ADLs serve as standard benchmarks found in commonly used HAR datasets, including *Opportunity* [11], UCI-HAR [3], and WISDM [47]. To push the boundaries beyond these foundational tasks, we incorporated sports activities that introduce a higher degree of complexity through high-intensity, variable movements. Training a model on these dynamic actions forces it to learn more sophisticated and generalizable features, thereby enhancing the dataset's value for emerging applications in sports science and digital coaching.

To manage this complexity and create a focused dataset for analysis, we adopted a specific data collection strategy for the sports activities. Rather than recording long, continuous sequences of gameplay (e.g., a full basketball sequence involving dribbling, crossover, and layup), we captured several repetitions of a single, fundamental action from multiple participants. For instance, we focused on the distinct motion of passing a basketball, a frequently used and representative movement.

4.3.3 Campaign 3 (Sentiment). For sentiment data collection, we considered six sentiment types: focus, distraction, stress, relaxation, depression, and excitement. The primary goal of choosing these sentiment types was to move beyond simplistic, one-dimensional sentiment analysis (such as positive, negative, or neutral) and instead capture a multi-faceted snapshot of an individual's psycho-emotional and cognitive state. This approach is intended to contribute to the development of mental health technology, remote monitoring, and elderly care, particularly for those who live alone.

These sentiment form three key pairs, each representing a fundamental axis of human experience. The focus-distraction axis offers insight into attentional state and cognitive load, which are critical indicators of mental performance. The stress-relaxation axis reflects the state of the autonomic nervous system and physiological responses to pressure. Finally, the depression-excitement axis addresses both persistent negative moods and positive engagement, which are important for evaluating overall quality of life.

We split the data collection into two parts. In Part I, we collected a continuous recording for the first two pairs (focus-distraction; stress-relaxation), approximately 10 to 12 minutes per participant without interruptions between the different stages. Part II focus on the recording of depression-excitement. In this campaign, we have 23 participants.

Part I.: The participant was seated at a large desk, approximately 2 meters wide, with a chair. The primary task was to assemble a jigsaw puzzle (see Fig. 9). The puzzle pieces were intentionally scattered across the wide desk surface. This design choice was made to encourage participants to make large, deliberate, and easily detectable movements with their arms and upper body when searching for and reaching for pieces, providing rich data for the motion sensors.

The 10-12 minute campaign was structured into four consecutive phases, each designed to induce a specific target state:

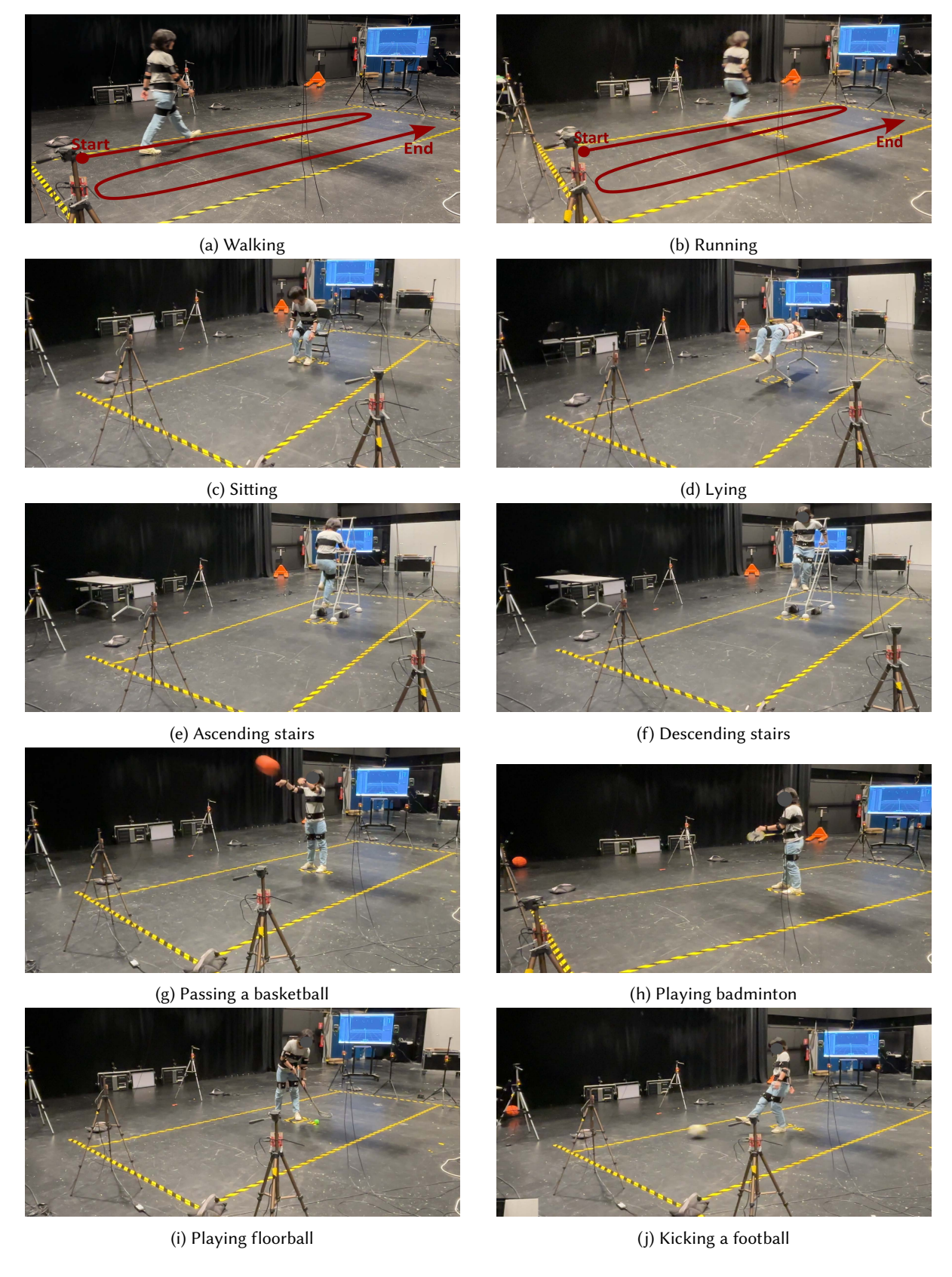


Fig. 8. Human activities set for Campaign 2.



Fig. 9. Experimental setup for Part I sentiment data collection: assemble a jigsaw puzzle.

- (1) Focus Phase (2 minutes): This initial phase served as a baseline. The participant was simply instructed to begin assembling the jigsaw puzzle at their own pace, without any external pressures or interruptions. This was designed to capture a state of natural concentration on the task.
- (2) Distraction Phase (3-5 minutes): To trigger a state of distraction, a series of escalating interruptions was introduced while the participant continued the puzzle task. The interruptions were layered in three levels: Level 1: Auditory distractions were introduced, including random background noises and a phone ringtone played every 30 seconds; Level 2: Verbal interruptions were added on top of the auditory distractions; Level 3: While the auditory and verbal distractions continued, three data recorders began engaging in sports activities within the experiment room to create a physical distraction.
- (3) Stress Phase (3 minutes): The participant was verbally informed, "You have now only 3 minutes to finish it." This was reinforced with two additional stressors: a large countdown timer was displayed on a screen in front of the participant; verbal countdowns were announced, including an oral reminder for the final 30 seconds.
- (4) Relaxation Phase (2 minutes): In the final phase, the stressors were removed. The participant was explicitly told that the time pressure was gone and that they could continue building the puzzle at their own speed.

Part II. : The second part of the data collection aimed to record behaviors associated with depression and excitement through a role-playing methodology. To avoid inducing genuine distress, participants viewed video stimuli to help them understand and simulate a target emotion, which they were then asked to embody during the recording.

For the depression task, participants watched a short video that personified the emotion. For the contrasting excitement task, they viewed a high-energy video, with the option to choose a clip they personally found motivating (e.g., rock climbing). After each video, they responded to neutral prompts, such as "Describe an experience with sports," by role-playing the target emotion through their speech, tone of voice, and body language.

Two important considerations were noted for this phase. First, the semantic content of the participants' stories was not subject to analysis; the focus was exclusively on the expressive, non-verbal cues in their speech and body language. Second, participants were encouraged to speak in their preferred language to ensure they could express themselves naturally and comfortably.

Post-Task Assessment (Ground Truth Collection). Immediately after the recording task was completed, participants were asked to provide a self-assessment of their experience (see Tab. 3). They rated the intensity of each of the six target states (focus, distraction, stress, relaxation, depression, and excitement) they experienced during the relevant phases of the experiment. This self-reported data can serve as the detailed ground truth label for the sensor data collected during each phase. The ratings were provided on a 6-point likert scale from 0 to 5, with the following anchors:

- **0**: Not in the mood
- **1:** Slightly in the mood
- 2: Somewhat in the mood
- 3: Moderately in the mood
- **4:** Mostly in the mood
- **5:** Quite in the mood

4.3.4 Campaign 4 (Gestures). A total of 7,140 gesture instances were recorded from 17 volunteers (10 male and 7 female) with heights ranging from 155 cm to 185 cm. Each participant executed 21 hand gestures, repeating each gesture 20 times. All gestures were performed at two different distances from the antenna: 1.5 and 3 meters. The duration of individual gestures differed depending on both the complexity of the movement and the participant's execution speed.

Data samples from Radar, RFID, LoRa, IMU and Infrared Camera are shown in Fig. 14, Fig. 15, Fig. 16, Fig. 17 and Fig. 18, respectively. For LoRa, the figure provides an example of data encoding with SF = 6. In this case, a chirp can encode data using 64 different starting frequencies, e.g., 0 to 63.

# 4.4 On-body Sensor Setup

In addition to the sensors placed in the environment, different sensors were also placed at different body locations of the subject (see Fig. 10, Fig. 11, and Fig. 12). We considered three types of sensors attached to the human body:

- (1) RFID tags (shown in green in the figures): These tags are used for tracking and are placed on each arm—on the wrist (A2, A6), below the elbow (A3, A7), and above the elbow on the front side (A4, A8).
- (2) Infrared camera markers (shown in vellow): These markers are positioned to facilitate motion capture. The placement of the infrared camera markers varies across different campaigns.
- (3) IMU sensors (shown in gray): These sensors provide data on orientation, acceleration, and angular velocity. The placement of the IMU sensors varies across different campaigns.

Specifically, for Campaign 4 (Gestures), we have two additional tags (A1 and A5) placed on the wrists of both hands (see Fig. 7).

Tab. 4 details the sensor placement for each campaign. Across all experiments, eight RFID tags were consistently used. The placement of IMU sensors varied by campaign. For Campaign 1 (gesture collection) and Campaign 3 (sentiment collection), sensors were placed exclusively on the upper body (chest, left and right arms), as these experiments were designed to capture upper-body motion. In contrast, for Campaign 2, IMU data were collected from the right arm, chest, and right leg.

Camera markers were placed to help the studio's infrared camera system capture movements from desired body locations. For the gesture data in Campaign 1, markers were limited to the upper body. For the other campaigns, they were placed on the arms, chest, hip, and legs. It is important to note a limitation regarding

Table 3. Campaign 3 - Emotional & Cognitive State Self-Assessment. Scale Key: 0=Not in the mood; 1=Slightly; 2=Somewhat; 3=Moderately; 4=Mostly; 5=Quite in the mood.

User ID		Pa	Part II			
OSCI ID	Focus	Distraction	Stress	Relaxation	Depression	Excitement
U01	-	-	-	-	-	-
U03	4	3	3	4	3	3
U04	4	3	4	2	-	3
U05	-	-	-	-	-	-
U06	4	4	3	3	3	3
U07	5	3	3	3	5	3
U08	3	2	1	3	4	5
U10	4	3	4	5	-	-
U11	5	2	2	3	2	5
U12	4	4	3	3	4	4
U13	4	3	4	5	3	2
U14	4	2	3	5	5	4
U17	4	4	3	3	2	4
U19	-	-	-	-	-	-
U21	4	3	5	3	2	3
U22	4	4	4	3	4	5
U24	4	3	2	5	3	4
U25	4	3	4	4	-	-
U28	-	-	-	-	-	-
U29	4	1	1	3	3	1
U30	4	5	4	5	3	4
U32	4	2	1	4	3	2
U33	5	4	4	3	4	3
U35	3	2	2	3	3	2
U36	-	-	-	-	-	-
U38	4	2	2	3	1	2
U41	4	3	3	4	4	3
U42	-	-	-	-	-	-
U44	4	1	1	5	3	5

Campaign 3. During the first part of this campaign, participants were seated at a desk to complete a puzzle. The desk obstructed the cameras' view. Thus, the marker data from this segment is unusable for analysis.

# 4.5 Participant Information

A total of 44 subjects participated in our data collection, consisting of 27 male and 17 female participants (see Tab. 5). Not all of them participated in all campaigns. There were 25 subjects for Campaign 1 and Campaign 2, 23 subjects for Campaign 3 and 17 subjects for Campaign 4. The group was predominated by the 21-30 age range. The study also included five younger participants (three of whom were under 18, for whom we obtained signed







Campaign 1: gesuture collection.

Fig. 10. On-body sensor placement for Fig. 11. On-body sensor placement for Fig. 12. On-body sensor placement for Campaign 2: human activity collection. Campaign 3: sentiment collection.

Table 4. Sensor placement

	Sensor placement					
	Campaign 1	Campaign 2	Campaign 3	Campaign 4		
RFID Tag - Left arm	✓	✓	✓	✓		
RFID Tag - Right arm	$\checkmark$	$\checkmark$	$\checkmark$	$\checkmark$		
Radar - Floor (8)	$\checkmark$	$\checkmark$	$\checkmark$	-		
Radar - Ceiling (5)	$\checkmark$	$\checkmark$	✓	-		
IMU - Left arm	$\checkmark$	-	✓	-		
IMU - Right arm	$\checkmark$	$\checkmark$	✓	-		
IMU - Chest	$\checkmark$	$\checkmark$	✓	-		
IMU - Right leg	-	$\checkmark$	-	-		
Camera markers - Left arm	$\checkmark$	$\checkmark$	✓	-		
Camera markers - Right arm	$\checkmark$	$\checkmark$	✓	-		
Camera markers - Chest	$\checkmark$	$\checkmark$	✓	-		
Camera markers - Left leg	-	$\checkmark$	$\checkmark$	-		
Camera markers - Right leg	-	$\checkmark$	$\checkmark$	-		
Camera markers - Hips	-	$\checkmark$	$\checkmark$	-		

parental consent) and a smaller number of individuals between the ages of 31 and 50. Additionally, we collected arm length information from our participants to provide valuable context for the analysis.

## 4.6 Data Statistics

Fig. 19 reveals that the campaigns operate on entirely distinct time scales and exhibit unique distribution patterns. Campaign 1 (gestures) shows tight clustering with a mean of 3.51 seconds and median of 3.29 seconds, representing quick, discrete physical movements from the arm. Campaign 2 (activity) displays moderate durations with a mean of 5.92 seconds and median of 3.89 seconds, indicating more complex behaviors that still remain relatively brief. Campaign 3 (sentiment) operates on a dramatically different scale with a mean of 154.03 seconds and a

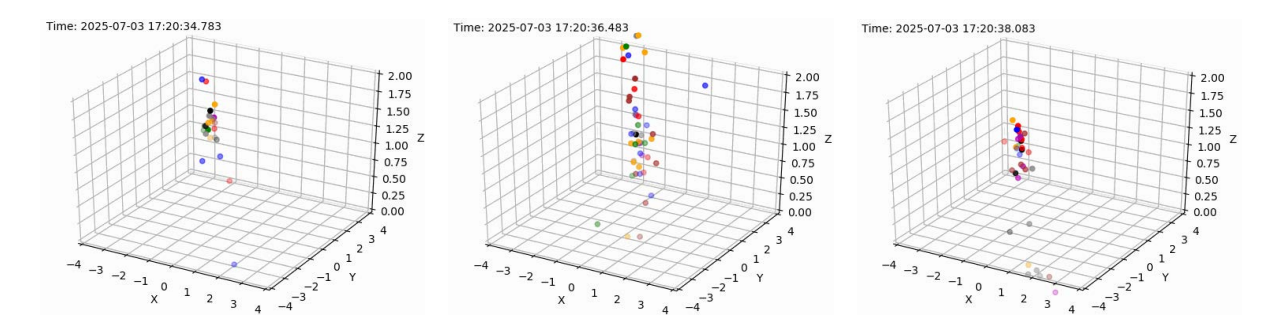


Fig. 13. Examples of aggregated sample data collected by radars mounted on the ground.

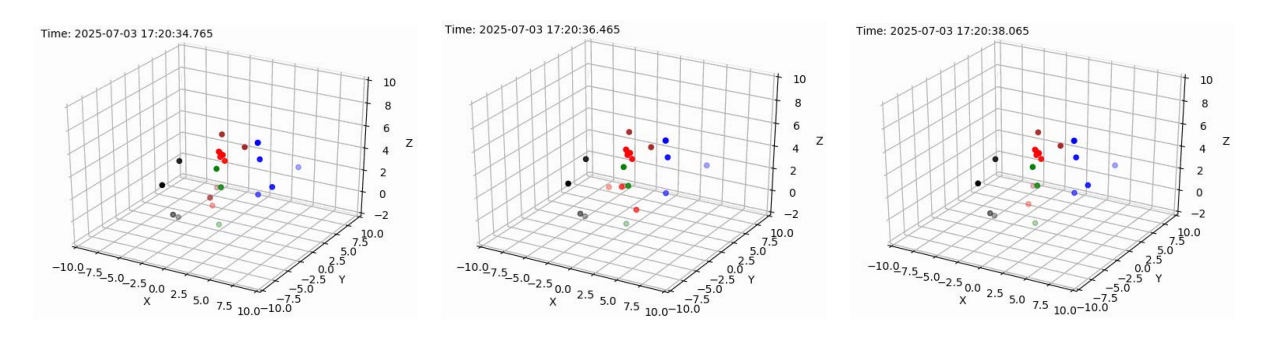


Fig. 14. Examples of aggregated sample data collected by radars mounted on the ceiling.

// 04/07/2025 12.05.20							
// ReaderName=Speedwayr-15-32-c2	AntennalDs=1	InventoryMode=DualTarget	ModeIndex=1003	Population=32	PowerInDbm=31	5	Session=2
// Timestamp	EPC	TID	Antenna	RSSI	Frequency	Hostname	PhaseAngle
2025-07-04T12:16:51.9602870+03:00	A700000000000000000000000		1	-65	865,7	Speedwayr-15-32-c2	28,532,042,654,672,900
2025-07-04T12:16:52.1057930+03:00	A6000000000000000000000000000000000000		1	-61	865,7	Speedwayr-15-32-c2	58,659,425,328,746,900
2025-07-04T12:16:52.1849350+03:00	A6000000000000000000000000000000000000		1	-60,5	865,7	Speedwayr-15-32-c2	6,261,709,576,149,180
2025-07-04T12:16:52.2297910+03:00	A4000000000000000000000000000000000000		1	-60	865,7	Speedwayr-15-32-c2	2,000,310,947,402,870
2025-07-04T12:16:52.2331760+03:00	A6000000000000000000000000000000000000		1	-61,5	865,7	Speedwayr-15-32-c2	0,1564660403643354
2025-07-04T12:16:52.2562540+03:00	A4000000000000000000000000000000000000		1	-60	865,7	Speedwayr-15-32-c2	5,184,855,063,053,460
2025-07-04T12:16:52.2724730+03:00	A6000000000000000000000000000000000000		1	-62	865,7	Speedwayr-15-32-c2	3,497,476,196,379,260
2025-07-04T12:16:52.3019760+03:00	A4000000000000000000000000000000000000		1	-59,5	865,7	Speedwayr-15-32-c2	2,030,990,563,160,580

Fig. 15. A example of collected data from RFID. The key features are timestamp, Electronic Product Code (EPC), the Received Signal Strength (RSS), and the signal phase

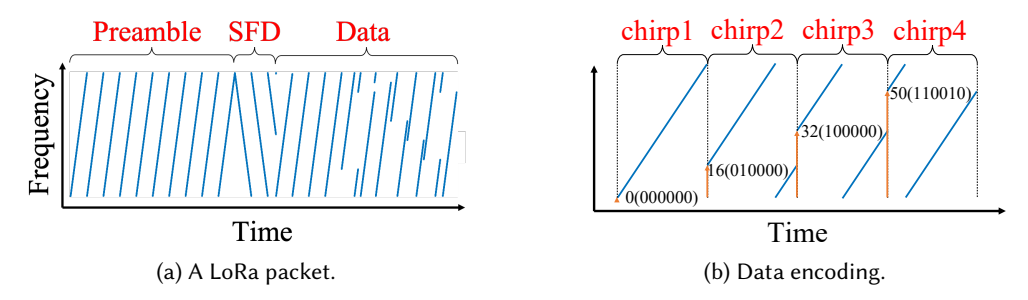


Fig. 16. Illustration of LoRa signal spectrum.

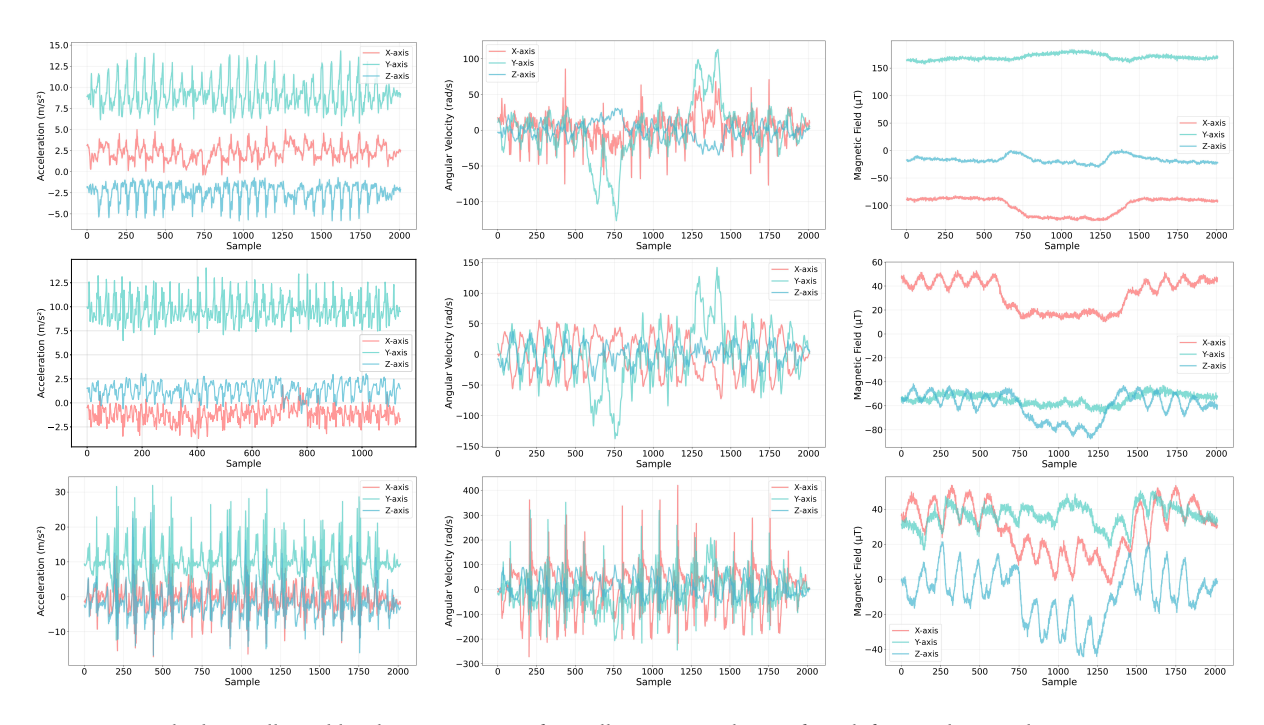


Fig. 17. Sample data collected by the IMU sensors for walking. For each row, from left  $\rightarrow$  right: Accelerometer, Gyroscope and Magnetometer. From top  $\rightarrow$  bottom: Chest, Right Arm, Right Leg.

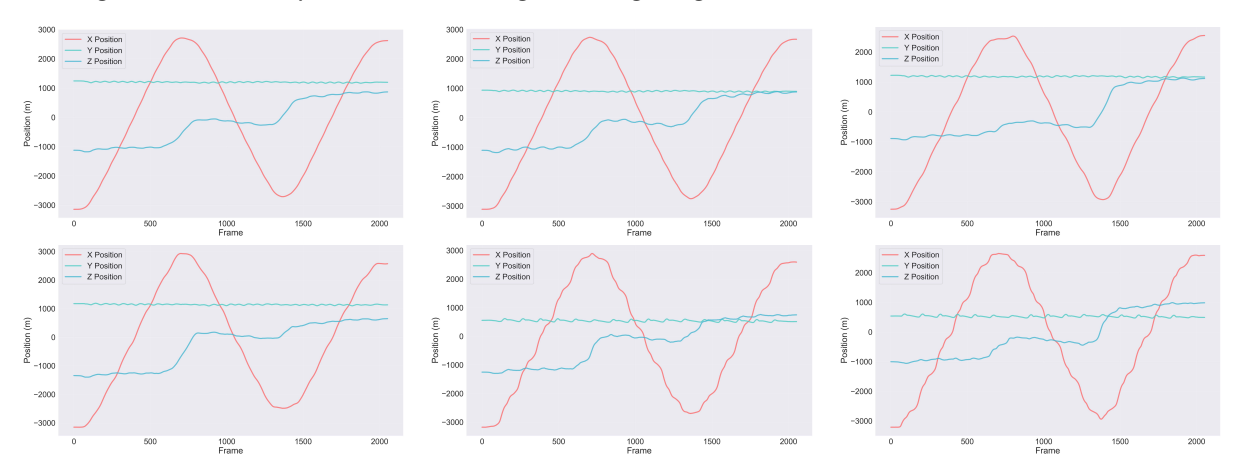


Fig. 18. Examples of sample data collected from different body locations by the infrared camera during walking. Top row: chest, hips, left arm; Bottom row: right arm, left leg, right leg. The camera system tracked markers attached to various body parts within the capture space. The visualizations from different body locations appear similar because all markers remain in close proximity to one another on the body, and their relative distances are small compared to the overall displacement of the participant during walking.

Table 5. Participant Information and Campaign Completion Status.

UserID	Gender	AgeRange	ArmLength (cm)	Campaign 1	Campaign 2	Campaign 3	Campaign 4
U01	F	41-50	57	✓	✓	-	-
U02	F	21-30	57	-	-	-	✓
U03	M	21-30	58	✓	✓	✓	-
U04	M	21-30	54	✓	✓	✓	-
U05	M	21-30	54	✓	✓	-	-
U06	M	21-30	58	✓	✓	✓	-
U07	F	21-30	53	✓	✓	✓	-
U08	F	21-30	52	_	_	✓	-
U09	M	21-30	62	_	_	-	✓
U10	M	< 18	43	✓	✓	✓	-
U11	F	21-30	50	✓	✓	✓	_
U12	F	31-40	58	· /	· /	✓	_
U13	M	21-30	56	-	· /	· ✓	-
U14	F	18-20	52	✓	· /	· /	_
U15	M	21-30	62	-	-	-	✓
U16	M	21-30	64	_	_	_	· ✓
U17	M	21-30	52	✓	✓	✓	-
U18	M	21-30	70	-	-	-	1
U19	F	< 18	55	✓	1	_	-
U20	F	21-30	67	•	•	_	
U21	M	21-30	52	<u></u>	- ✓	- ✓	<b>V</b>
U22	M	21-30	58	<b>√</b>	<b>√</b>	<b>√</b>	-
U23	F	21-30	58	<b>V</b>	<b>V</b>	<b>V</b>	- ✓
U23 U24	г М	21-30	56 57	-	-	- ✓	<b>√</b>
U25	M	< 18	39	- -	- ✓	<b>√</b>	<b>V</b>
U25 U26	M M			<b>√</b>	<b>√</b>	<b>√</b>	-
	M M	21-30	64	-	-	-	✓ ✓
U27		21-30	70	-	-	-	
U28	M	41-50	55	✓ ,	✓,	-	✓
U29	F	31-41	49	✓	✓,	✓,	-
U30	M	21-30	53	-	$\checkmark$	✓	-
U31	F	21-30	57	-,	-,	<del>-</del>	✓
U32	M	21-30	59	✓.	✓.	✓.	-
U33	F	21-30	48	✓	✓	$\checkmark$	-
U34	F	21-30	52		-	-	✓
U35	M	18-20	50	✓	✓	✓	-
U36	M	21-30	-	✓	-	-	-
U37	M	21-30	67	-	-	-	✓
U38	M	21-30	57	✓	✓	✓	-
U39	M	21-30	74	-	-	-	✓
U40	M	21-30	75	-	-	-	✓
U41	F	21-30	54	✓	✓	✓	-
U42	F	21-30	52	✓	-	-	-
U43	F	21-30	61	-	-	-	✓
U44	M	21-30	56	✓	✓	✓	-

median of 121.63 seconds, representing sustained emotional expressions lasting over two minutes on average, which also aligns with the design of the experiment. This progression from seconds to minutes reflects increasing behavioral complexity and the transition from instantaneous actions to prolonged states.

For Campaign 1 (Motion Gestures), the violin plots reveal that most individual gestures maintain narrow distributions. The majority of gestures cluster in the 2-4 second range across the violin plots, with only a few motions (M10 - arm swing, M20 - circle-clockwise, M21 - circle-counter-circles) requiring extended durations, suggesting these represent either more complex multi-step movements or gestures requiring greater spatial displacement.

For Campaign 2, the histogram shows a dominant peak around 3-4 seconds but also reveals a significant secondary distribution extending from 15-25 seconds. This bimodality is strikingly apparent in the violin plots, where A01 (walking) and A02 (running) form a clearly separate cluster with distributions centered around 18-20 seconds and 10-12 seconds, respectively. This is also expected as for walking and running, the participants were asked to walk/run in an "S" shape within the recording area.

Campaign 3 shows an extremely wide distribution ranging from approximately 20 seconds to over 400 seconds. The histogram reveals a highly uneven distribution with the peak around 120 seconds, but with many instances extending well beyond 200 seconds. The large difference between the mean (154.03s) and median (121.63s) indicates that longer durations significantly pull the average upward. The violin plots reveal extreme heterogeneity across sentiment types, reflecting different experimental protocols for each emotion. E01 (focus) shows a concentrated distribution around 120 seconds, while E03 (stress) displays a concentrated distribution around 180 seconds. These patterns directly correspond to the experimental design, where we imposed time limits of 2 minutes for focus and 3 minutes for stress. E04 (relaxation) similarly shows a relatively narrow, consistent pattern around 120 seconds. In contrast, E05 and E06 display moderate durations with wide distributions spanning 50-250 seconds. This variability is reasonable and expected, as data collection for depression and excitement involved participants sharing personal stories while experiencing these emotions. The recorded length naturally varied depending on each participant's storytelling style, resulting in the observed distribution spread.

Compared with Campaign 1, data from Campaign 4 shows consistently shorter durations (47%). M10 (arm swing) in Campaign 4 is comparable to other motions (1.5-3 seconds, median 2s). These might due to the different participant instructions during the data collection.

#### Benchmarks and Baseline Results 5

The RF-Behavior dataset provides the opportunity for a multitude of use cases. Here, we focus on introducing one exemplary use case for radar and RFID: (1) radar-based gesture recognition (ground, ceiling, combination of ground and ceiling radars), as well as, (2) RFID-based gesture recognition.

Accuracy, macro-averaged  $F_1$ -score, area under the ROC curve (AUC), and normalized confusion matrix are used for evaluation. Accuracy reflects end-to-end gesture classification performance. The macro F<sub>1</sub>-score compensates for class imbalance between "easy" single-hand gestures and more complex two-hand or circular gestures. AUC is reported to quantify separability across classes at different decision thresholds. Confusion matrices highlight systematic confusions between visually/kinematically similar gestures (e.g., left-vs-right swipes or inward-vs-outward circular motions).

## 5.1 Radar-based Gesture Recognition

This section defines the radar-based gesture recognition benchmark for our dataset. All reported baselines are trained and tested on the radar point clouds collected in campaign 1 (gesture recording) using the same preprocessing, data split, optimization, and downstream pipeline settings.

Preprocessing pipeline: Radar point clouds contain background clutter, multipath reflections, and frame-to-frame variability in point density. A unified preprocessing protocol is applied to every recorded gesture instance before training any model. (1) Clutter suppression: For each gesture instance, all frames are first merged into a single aggregated point cloud. Using DBSCAN with  $\epsilon = 1$  and a minimum cluster size of 3, we segment the cloud and retain the largest high-density cluster, presumed to be the performer, while discarding minor clusters as noise; (2) Temporal normalization: To ensure consistent temporal structure for model input, each gesture instance is re-segmented into a fixed number of frames (e.g., 2, 4, or 8); (3) Point set normalization: We therefore Resample the original point-cloud for each frame to have target number of points.

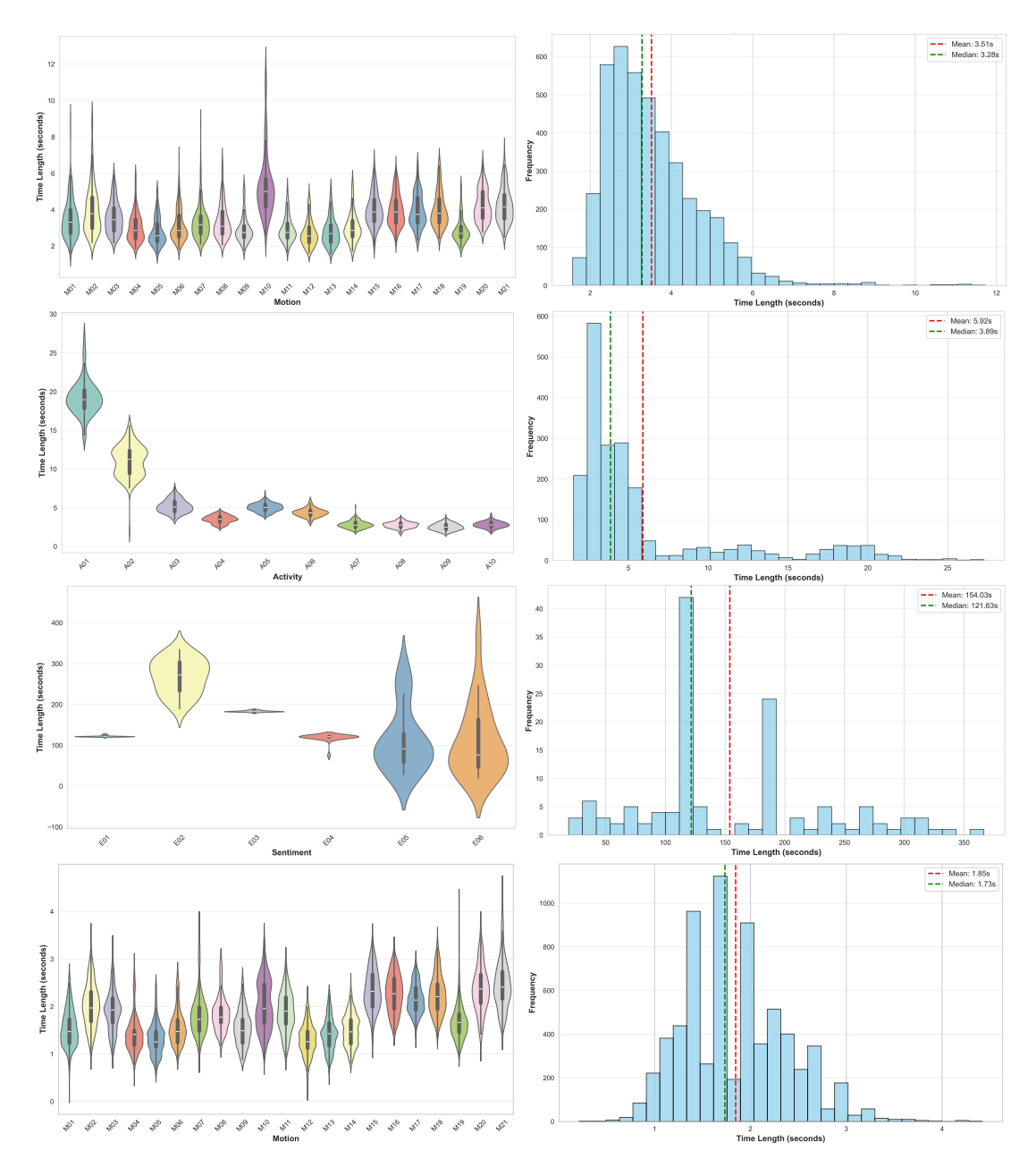


Fig. 19. From Top  $\rightarrow$  Bottom: Time length distribution for data from Campaign 1, 2, 3, 4.

Benchmark models: We include three representative models. PointNet++ [35] is a widely used hierarchical network for point cloud processing. It progressively aggregates local neighborhoods to learn both fine-grained and global spatial features directly from unordered points. Pantomime [34] combines a PointNet++-style spatial

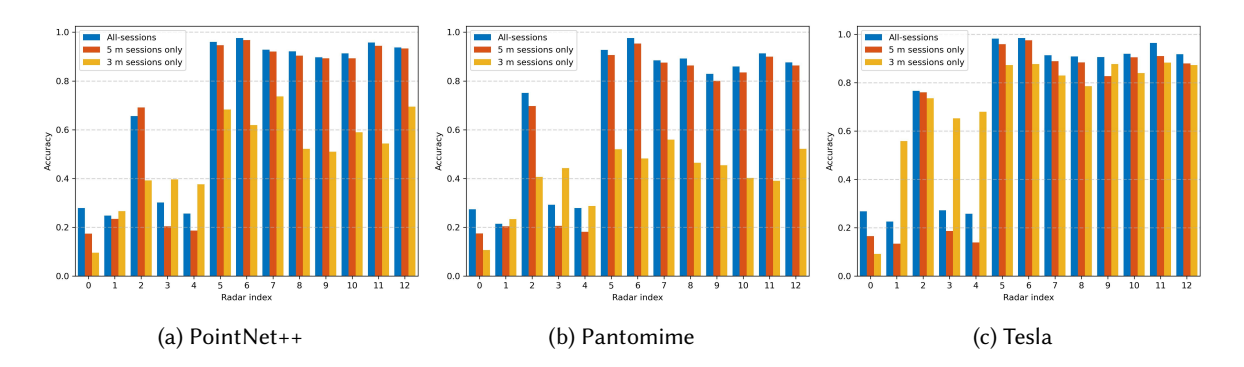


Fig. 20. Gesture recognition accuracy on benchmark models. From Left  $\rightarrow$  Right: Pointnet++, Pantomime, Tesla. The X-axis indicates the Radar Index (see Fig. 2) while the Y-axis shows the accuracy.

encoder with recurrent Long Short-Term Memory (LSTM) layers. PointNet++ operates on each frame to learn hierarchical geometric descriptors from sparse 3D points, and the LSTM stack captures the temporal dynamics across frames. **Tesla** [39] is a compact gesture recognition architecture tailored for mmWave radar. It extracts spatial features frame-by-frame from the radar point cloud and then models their temporal evolution over the gesture sequence.

Training and optimization: All experiments are implemented in PyTorch and run on an NVIDIA GeForce RTX 4080 GPU. We use Adam as the optimizer for all baseline models. To ensure fair comparison, we do *not* tune hyperparameters per model or per radar configuration. The same optimizer, schedule, patience, and batch construction strategy are used across Tesla, Pantomime, and PointNet++ in all three sensing settings (ground-only, ceiling-only, fusion). This design choice intentionally fixes the training recipe so that differences in performance primarily reflect sensing geometry and model architecture, rather than per-model tuning.

5.1.1 Radar-based Gesture Recognition. We split gesture data into three groups: all samples, 5-meter samples and 3-meter samples. As mentioned in Sec. 4.2, we adjusted the height of the radar placement on the ceiling from 5 meters to 3 meters during data collection. We first evaluated the gesture recognition performance using single radar.

Fig. 20 shows the results gesture recognition using data from single radar with different models (From Left → Right: Pointnet++, Pantomime and Tesla). The X-axis indicates the Radar Index (see Fig. 2) while the Y-axis shows the accuracy. Indexes 0-4 represent radars mounted on the ceiling, while the rest indicate those on the ground. For the radars on the ceiling, across all models, Radar 2 provides the highest accuracy for data from the 'All' and '5-meter' groups, while the accuracy for the '3-meter' group remains relatively low, similar to results from the other radars mounted on the ceiling. This could be because Radar 2 is positioned directly above the subject, capturing more information while the subject performs various gestures. As the other ceiling-mounted radars are relatively distant from the subject, they may not capture a sufficient amount of information. For the radars placed on the ground, PointNet++ and Pantomime models show poor performance with data from the '3-meter' group, which might due to the limited amount subjects in the group. In contrast, the Tesla model exhibits superior performance with the same group, even outperforming other models for radars placed on the ceiling. Fig. 21 provides the Confusion matrices for gesture recognition results using data from Radar 2 (left) and Radar 5 (right). For model trained on data from Radar 2 (placed right above the subject), it has significant low performace (less than 70%) on complex gestures: two-hand-push, two-hand-pull, left-arm-circle, two-hand-inward-circles, two-hand-ateral-to-front, circle-clockwise.

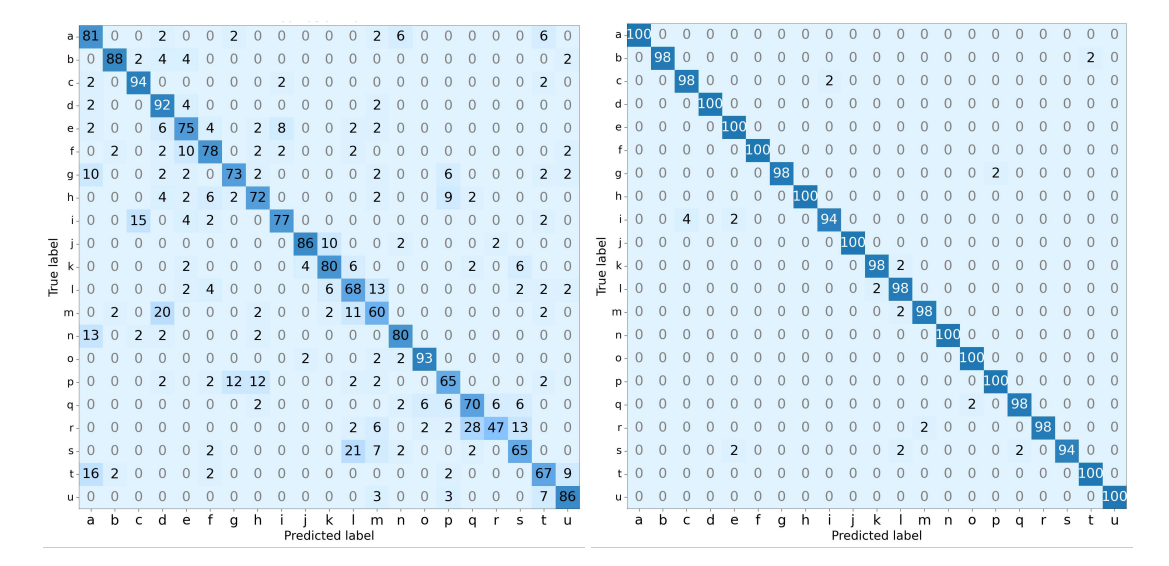


Fig. 21. Confusion matrices for gesture recognition results from Tesla model using data from Radar 2 (left, placed right above the subject) and Radar 5 (right, placed in front of the subject). Labels (a-u) on the X-axis and Y-axis represent the gestures.

Table 6. Gesture recognition accuracy (%) on different evaluation	settings with	ı Tesla model.
-------------------------------------------------------------------	---------------	----------------

Data Group	Ceiling-only	<b>Ground-only</b>	Ceiling+Ground
3-meter campaigns	85.02	99.11	99.01
5-meter campaigns	78.45	99.35	98.61
All campaigns	83.82	99.01	99.23

To reflect different deployment constraints, we define three evaluation settings:

- Ceiling-only: We use only the 5 ceiling-mounted radars. This provides a predominantly top-down view with reduced self-occlusion from the arms and torso. This setting is representative of ceiling-installed infrastructure in smart-room or smart-home scenarios.
- Ground-only: We aggregate only the point clouds from the 8 ground radars. It also matches common gesture-sensing setups where devices are placed around the user at approximately chest/arm height.
- Ceiling+Ground: We merge all available radars (8 ground + 5 ceiling) after time synchronization and coordinate alignment. This produces denser, more complete 3D point clouds with improved coverage of subtle hand/arm motion as well as full upper-body kinematics.

Tab. 6 presents the results of three different evaluation settings. The Ground-only setting achieves the best performance in both the '3-meter' and '5-meter' groups, while combining data from ceiling- and ground-mounted radars yields slightly better results in the 'All' group setting. Although using Ceiling-only data results in the lowest average accuracy, the performance remains acceptable, indicating the potential to replace ground-mounted radars with ceiling-mounted ones (a more user-friendly setting) in smart environments.

To further evaluate the contribution of gesture recognition enabled by ceiling-mounted radars, we combined Radar 2 with the radars positioned on the ground. The results indicate that integrating data from Radar 2 enhances the performance of ground radars, particularly those not placed directly in front of the subject (see Fig. 22).

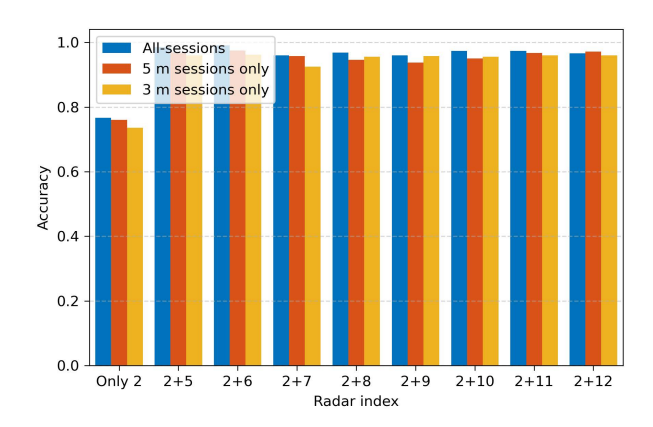


Fig. 22. Gesture recognition accuracy based on the combination of Radar 2 (from ceiling, directly above the subject) and radars on the ground (Indexes 5-12) using Tesla model.

Obvious improvements have been made for all data groups when comparing the result with single radar setting (see Fig. 20c) for radars with Indexes 6-12. Ceiling-mounted radars offer additional advantages such as reduced physical obstructions in the environment, improved coverage area, and increased flexibility in positioning, which can lead to more reliable gesture recognition. Furthermore, they provide the potential for capturing a holistic view of the interaction space, improving the overall robustness and accuracy of the system.

# 5.2 RFID-based Gesture Recognition

This section presents the RFID-based gesture recognition reference model and benchmark models evaluated using the data from Campaign 4. We utilize RSS and phase information reflected by the tags. The raw data from the reader is first processed. Specifically, this process includes data formatting, phase unwrapping, normalization, and managing missing data points.

*Preprocessing and Learning Framework:* Two types of missing data are identified. The first occurs when a tag temporarily disconnects during gesture execution, while the second arises when a tag is not detected at all for a given execution. Adaptive interpolation is employed to handle temporary disconnections, whereas within-class imputation combined with proximity-based imputation is applied to tackle completely missing tag data. Each recorded gesture consists of 8 dataframes, with each dataframe corresponding to a unique tag (identified by its EPC). Each dataframe contains 4 columns: timestamp, RSS, phase, and the tag's EPC.

For classification, we adopt the graph-based convolutional neural network proposed in [39]. A temporal K-nearest neighbors (K-NN) approach is used to construct a graph, where each EPC is represented as a node, and edges connect nodes based on the similarity of their RSS and phase values across successive timestamps. An edge is created between EPCs i and j if the prior reading of EPC i at time t-1, characterized by the RSS and phase pair  $(\alpha_i^{t-1}, \phi_i^{t-1})$ , falls within the K nearest neighborhood defined by the current reading of EPC j at time t,  $(\alpha_j^t, \phi_j^t)$ . In this way, each EPC is linked to its most similar counterparts at the following timestamp, capturing temporal correlations and enabling effective feature propagation across the graph.

Benchmark models: A Random Forest Classifier (RF) model developed by [48] is used as a benchmark, testing its performance with three feature configurations: features extracted from the phase signal alone (RF with SP); a combination of wavelet coefficients and statistics of phase (RF with SWP); and statistical features from both the phase and RSS signals (RF with SPR). Other established models are also utilized as benchmarks: Early Fusion

Method	Accuracy	Precision	Recall	F1-score
RF with SP	83.56	83.72	83.56	83.42
RF with SWP	86.26	86.48	86.2	86.07
RF with SPR	95.25	95.35	95.25	95.23
Early Fusion	83.62	84.25	83.57	83.34
Late Fusion	87.13	88.32	87.08	86.91
The reference model	98 13	98 19	98 13	98 13

Table 7. Evaluation scores (%) for RFID-based gesture recognition.

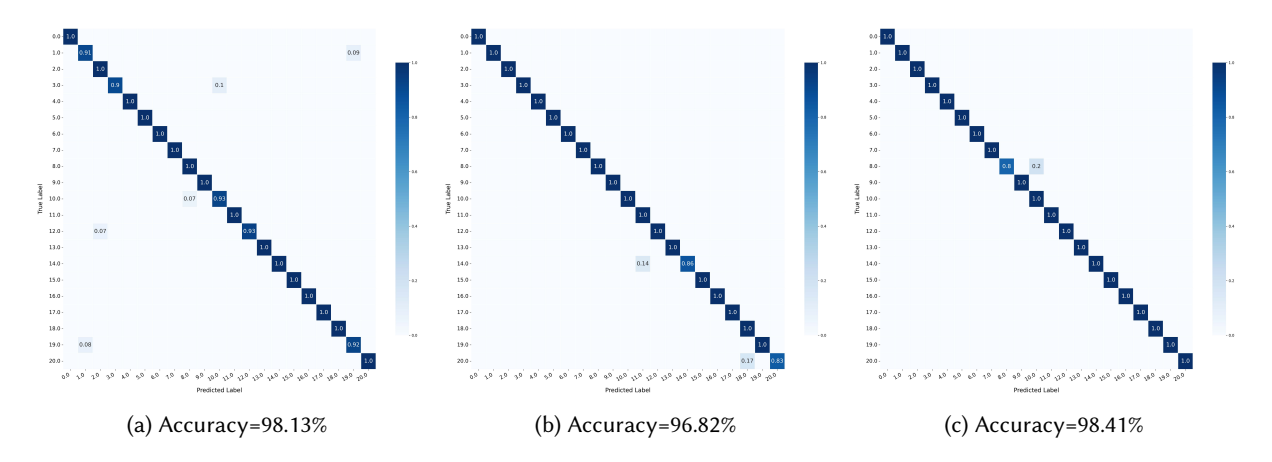


Fig. 23. Normalized confusion matrices produced by a reference model using the collected datasets: (a) Distance = 3 m, Environment A; (b) Distance = 1.5 m, Environment A; (c) Distance = 1.5 m, Environment B.

([10]), Late Fusion ([17]). Metrics including accuracy, precision, recall, and F1-score derived from the benchmarks and the reference model are presented in Tab. 7. As illustrated in Fig. 23, the confusion matrices for the complete set of gestures in the reference model indicate overall test accuracies of 98.13%, 96.82%, and 98.41% across the three datasets. Taking the first dataset as an example (see Fig. 23a), perfect classification was achieved for 16 gestures, while the remaining classes attained accuracies above 90%.

## 6 Discussion & Conclusion

We presented a comprehensive multimodal dataset, *RF-Behavior*, that integrates eight ground-mounted radars, five ceiling-mounted radars, RFID tags, LoRa, inertial measurement units (IMUs), and infrared cameras to capture human behavior across three distinct temporal and complexity scales: 21 hand gestures, 10 activities, and 6 sentiment expressions from 44 participants. By combining complementary sensing and a broad behavioral catagories, the dataset enables research on viewpoint-robust RF perception, multimodal fusion under occlusion and poor lighting, and cross-task learning between motion and emotion domains. The benchmark results obtained using radars (groud- and ceiling-mounted) and RFID tags shows how these modalities offers strengths in related tasks.

This dataset enables rich multimodal fusion and representation learning by combining multi-angle radar, RFID, IMU, and infrared time series dataset, which opens several concrete directions for advancing multimodal sensing, modeling, and deployment. A central opportunity is viewpoint robustness and angle-invariant recognition.

With synchronized ground and ceiling radar views, models can be trained to generalize across perspectives, reducing the need for site-specific calibration. Moreover, a proper installation of ceiling radar could possible remove the need of ground radars, proving angle-invariant recognition with more user-friendly hardware setup. Large-scale self-supervised objectives—such as masked time-frequency modeling or cross-modal alignment—can learn transferable features that adapt rapidly to new rooms, sensor layouts, or behaviors with few labels. By joint modeling of motion and emotion, we can separate how a person feels from what they are doing, and estimate emotion continuously over time. This helps us understand how emotions change the people motion in real-life settings. Applications include sentiment-aware smart spaces that adapt lighting or notifications to user state, and privacy-preserving wellbeing monitoring that detects stress or agitation without identifiable vision information, which is important for healthcare, eldercare, and workplace wellbeing.

There are also limits. While 44 participants add variety, a larger and more diverse group would help models generalize better. The recordings were made in a controlled indoor lab, and the gestures, activities, and emotions were performed according to a fixed protocol, which may differ from everyday behavior. Collecting data "in the wild" would complement this setup and provide insights into a model's effectiveness in varied, uncontrolled environments.

# **Dataset Availability**

The use of the RF-Behavior is limited to academic research purposes. The dataset is publicly available at [https: //www.kaggle.com/datasets/anonymizers/rf-behavior-dataset]. The sample code used for data processing will also be provided.

### References

- [1] Shahzad Ahmed, Dingyang Wang, Junyoung Park, and Sung Ho Cho. 2021. UWB-gestures, a public dataset of dynamic hand gestures acquired using impulse radar sensors. Scientific Data 8, 1 (2021), 102.
- [2] Arnon Amir, Brian Taba, David Berg, Timothy Melano, Jeffrey McKinstry, Carmelo Di Nolfo, Tapan Nayak, Alexander Andreopoulos, Guillaume Garreau, Marcela Mendoza, et al. 2017. A low power, fully event-based gesture recognition system. In Proceedings of the IEEE conference on computer vision and pattern recognition. 7243-7252.
- [3] Davide Anguita, Alessandro Ghio, Luca Oneto, Xavier Parra, Jorge Luis Reyes-Ortiz, et al. 2013. A public domain dataset for human activity recognition using smartphones.. In Esann, Vol. 3. 3-4.
- [4] Sizhen Bian, Vitor Fortes Rey, Siyu Yuan, and Paul Lukowicz. 2022. The contribution of human body capacitance/body-area electric field to individual and collaborative activity recognition. arXiv preprint arXiv:2210.14794 (2022).
- [5] Marius Bock, Hilde Kuehne, Kristof Van Laerhoven, and Michael Moeller. 2024. WEAR: An Outdoor Sports Dataset for Wearable and Egocentric Activity Recognition. Proc. ACM Interact. Mob. Wearable Ubiquitous Technol. (IMWUT) 8, 4, Article 175 (2024), 21 pages. doi:10.1145/3699776
- [6] Mohammud J Bocus, Wenda Li, Shelly Vishwakarma, Roget Kou, Chong Tang, Karl Woodbridge, Ian Craddock, Ryan McConville, Raul Santos-Rodriguez, Kevin Chetty, et al. 2022. OPERAnet, a multimodal activity recognition dataset acquired from radio frequency and vision-based sensors. Scientific data 9, 1 (2022), 474.
- $\cite{Corentin Bouton. 2024. RFID-tags-detection. https://github.com/corentinbouton/RFID-tags-detection.}$
- [8] Carlos Busso, Murtaza Bulut, Chi-Chun Lee, Abe Kazemzadeh, Emily Mower, Samuel Kim, Jeannette N Chang, Sungbok Lee, and Shrikanth S Narayanan. 2008. IEMOCAP: Interactive emotional dyadic motion capture database. Language resources and evaluation 42,
- [9] Fabian Caba Heilbron, Victor Escorcia, Bernard Ghanem, and Juan Carlos Niebles. 2015. Activitynet: A large-scale video benchmark for human activity understanding. In Proceedings of the ieee conference on computer vision and pattern recognition. 961-970.
- [10] Francisco M Calatrava-Nicolás and Oscar Martinez Mozos. 2023. Light residual network for human activity recognition using wearable sensor data. IEEE Sensors Letters 7, 10 (2023), 1-4.
- [11] Ricardo Chavarriaga, Hesam Sagha, Alberto Calatroni, Sundara Tejaswi Digumarti, Gerhard Tröster, José del R Millán, and Daniel Roggen. 2013. The Opportunity challenge: A benchmark database for on-body sensor-based activity recognition. Pattern Recognition Letters 34, 15 (2013), 2033-2042.
- [12] Chen Chen, Roozbeh Jafari, and Nasser Kehtarnavaz. 2015. UTD-MHAD: A multimodal dataset for human action recognition utilizing a depth camera and a wearable inertial sensor. In 2015 IEEE International conference on image processing (ICIP). IEEE, 168-172.

- [13] Quentin De Smedt, Hazem Wannous, Jean-Philippe Vandeborre, Joris Guerry, Bertrand Le Saux, and David Filliat. 2017. Shrec'17 track: 3d hand gesture recognition using a depth and skeletal dataset. In 3DOR-10th Eurographics workshop on 3D object retrieval. 1–6.
- [14] Jacob Devlin, Ming-Wei Chang, Kenton Lee, and Kristina Toutanova. 2019. Bert: Pre-training of deep bidirectional transformers for language understanding. In *Proceedings of the 2019 conference of the North American chapter of the association for computational linguistics: human language technologies, volume 1 (long and short papers).* 4171–4186.
- [15] Paul Ekman. 1992. An argument for basic emotions. Cognition & Emotion 6, 3-4 (1992), 169-200.
- [16] Sahar Golipoor and Stephan Sigg. 2024. Environment and Person-independent Gesture Recognition with Non-static RFID Tags Leveraging Adaptive Signal Segmentation. In 2024 IEEE 29th International Conference on Emerging Technologies and Factory Automation (ETFA). IEEE, 1–8.
- [17] Sahar Golipoor and Stephan Sigg. 2024. RFID-based Human Activity Recognition Using Multimodal Convolutional Neural Networks. In 2024 IEEE 29th International Conference on Emerging Technologies and Factory Automation (ETFA). IEEE, 1–6.
- [18] Isabelle Guyon, Vassilis Athitsos, Pat Jangyodsuk, and Hugo Jair Escalante. 2014. The ChaLearn gesture dataset (CGD 2011). *Machine Vision and Applications* 25, 8 (2014), 1929–1951.
- [19] Eiji Hayashi, Jaime Lien, Nicholas Gillian, Leonardo Giusti, Dave Weber, Jin Yamanaka, Lauren Bedal, and Ivan Poupyrev. 2021. Radarnet: Efficient gesture recognition technique utilizing a miniature radar sensor. In Proceedings of the 2021 CHI Conference on Human Factors in Computing Systems. 1–14.
- [20] Jinhyeok Jang, Dohyung Kim, Cheonshu Park, Minsu Jang, Jaeyeon Lee, and Jaehong Kim. 2020. ETRI-activity3D: A large-scale RGB-D dataset for robots to recognize daily activities of the elderly. In 2020 IEEE/RSJ International Conference on Intelligent Robots and Systems (IROS). IEEE, 10990–10997.
- [21] Alexander Kapitanov, Karina Kvanchiani, Alexander Nagaev, Roman Kraynov, and Andrei Makhliarchuk. 2024. HaGRID-HAnd Gesture Recognition Image Dataset. In *Proceedings of the IEEE/CVF Winter Conference on Applications of Computer Vision*. 4572–4581.
- [22] Will Kay, Joao Carreira, Karen Simonyan, Brian Zhang, Chloe Hillier, Sudheendra Vijayanarasimhan, Fabio Viola, Tim Green, Trevor Back, Paul Natsev, et al. 2017. The kinetics human action video dataset. arXiv preprint arXiv:1705.06950 (2017).
- [23] Nicolai Kern, Daniel Laqua, and Christian Waldschmidt. 2023. A Dataset for Radar-based Traffic Gesture Recognition with Out-of-Distribution Detection. In 2023 20th European Radar Conference (EuRAD). 242–245. doi:10.23919/EuRAD58043.2023.10289248
- [24] Faheem Khan and Sung Ho Cho. 2019. Radar for health care: Recognizing human activities and monitoring vital signs. *IEEE Microwave Magazine* 20, 1 (2019), 66–78.
- [25] Sander Koelstra, Christian Muhl, Mohammad Soleymani, Jong-Seok Lee, Ashkan Yazdani, Touradj Ebrahimi, Thierry Pun, Anton Nijholt, and Ioannis Patras. 2011. Deap: A database for emotion analysis; using physiological signals. IEEE transactions on affective computing 3, 1 (2011), 18–31.
- [26] Jennifer R Kwapisz, Gary M Weiss, and Samuel A Moore. 2011. Activity recognition using cell phone accelerometers. ACM SigKDD Explorations Newsletter 12, 2 (2011), 74–82.
- [27] Hugo Landaluce, Laura Arjona, Asier Perallos, Francisco Falcone, Ignacio Angulo, and Florian Muralter. 2020. A review of IoT sensing applications and challenges using RFID and wireless sensor networks. Sensors 20, 9 (2020), 2495.
- [28] Shan Li, Weihong Deng, and JunPing Du. 2017. Reliable Crowdsourcing and Deep Locality-Preserving Learning for Expression Recognition in the Wild. In 2017 CVPR. IEEE, 2584–2593.
- [29] Jaime Lien, Nicholas Gillian, M Emre Karagozler, Patrick Amihood, Carsten Schwesig, Erik Olson, Hakim Raja, and Ivan Poupyrev. 2016. Soli: Ubiquitous gesture sensing with millimeter wave radar. ACM Transactions on Graphics (TOG) 35, 4 (2016), 1–19.
- [30] Haipeng Liu, Yuheng Wang, Anfu Zhou, Hanyue He, Wei Wang, Kunpeng Wang, Peilin Pan, Yixuan Lu, Liang Liu, and Huadong Ma. 2020. Real-time arm gesture recognition in smart home scenarios via millimeter wave sensing. *IMWUT* 4, 4 (2020), 1–28.
- [31] Jian Liu, Yan Wang, Yingying Chen, Jie Yang, Xu Chen, and Jerry Cheng. 2020. Wireless sensing for human activity: A survey. IEEE Communications Surveys & Tutorials 22, 3 (2020), 1629–1645.
- [32] Ali Mollahosseini, Behzad Hasani, and Mohammad H Mahoor. 2017. Affectnet: A database for facial expression, valence, and arousal computing in the wild. *IEEE Transactions on Affective Computing* 10, 1 (2017), 18–31.
- [33] Bao Ricky Nhan and Tom Chau. 2010. Classifying affective states using thermal infrared imaging of the human face. In *IEEE Transactions on Biomedical Engineering*, Vol. 57. 979–987.
- [34] Sameera Palipana, Dariush Salami, Luis A Leiva, and Stephan Sigg. 2021. Pantomime: Mid-air gesture recognition with sparse millimeter-wave radar point clouds. Proceedings of the ACM on interactive, mobile, wearable and ubiquitous technologies 5, 1 (2021), 1–27.
- [35] Charles Ruizhongtai Qi, Li Yi, Hao Su, and Leonidas J Guibas. 2017. Pointnet++: Deep hierarchical feature learning on point sets in a metric space. Advances in neural information processing systems 30 (2017).
- [36] Attila Reiss and Didier Stricker. 2012. Introducing a new benchmarked dataset for activity monitoring. In 2012 16th international symposium on wearable computers. IEEE, 108–109.
- [37] Fabien Ringeval, Andreas Sonderegger, Juergen Sauer, and Denis Lalanne. 2013. Introducing the RECOLA multimodal corpus of remote collaborative and affective interactions. In 2013 10th IEEE international conference and workshops on automatic face and gesture recognition (FG). IEEE, 1–8.

- [38] Daniel Roggen, Alberto Calatroni, Mirco Rossi, Thomas Holleczek, Kilian Förster, Gerhard Tröster, Paul Lukowicz, David Bannach, Gerald Pirkl, Alois Ferscha, et al. 2010. Collecting complex activity datasets in highly rich networked sensor environments. In 2010 Seventh international conference on networked sensing systems (INSS). IEEE, 233-240.
- [39] Dariush Salami, Ramin Hasibi, Sameera Palipana, Petar Popovski, Tom Michoel, and Stephan Sigg. 2022. Tesla-rapture: A lightweight gesture recognition system from mmwave radar sparse point clouds. IEEE Transactions on Mobile Computing 22, 8 (2022), 4946-4960.
- [40] Dariush Salami, Ramin Hasibi, Stefano Savazzi, Tom Michoel, and Stephan Sigg. 2024. Angle-Agnostic Radio Frequency Sensing Integrated Into 5G-NR. IEEE Sensors Journal (2024).
- [41] Philip Schmidt, Attila Reiss, Robert Duerichen, Claus Marberger, and Kristof Van Laerhoven. 2018. Introducing WESAD, a multimodal dataset for wearable stress and affect detection. In ACM ICMI. 400-408.
- $Meisam\ J\ Sekiavandi,\ Laurits\ Dixen,\ Jostein\ Fimland,\ Sree\ Keerthi\ Desu,\ Antonia-Bianca\ Zserai,\ Ye\ Sul\ Lee,\ Maria\ Barrett,\ and\ Paolo$ Burelli. 2025. Advancing Face-to-Face Emotion Communication: A Multimodal Dataset (AFFEC). arXiv preprint arXiv:2504.18969 (2025).
- [43] Amir Shahroudy, Jun Liu, Tian-Tsong Ng, and Gang Wang. 2016. NTU RGB+D: A large scale dataset for 3D human activity analysis. In  $Proceedings\ of\ the\ IEEE\ conference\ on\ computer\ vision\ and\ pattern\ recognition.\ 1010-1019.$
- [44] Akash Deep Singh, Sandeep Singh Sandha, Luis Garcia, and Mani Srivastava. 2019. Radhar: Human activity recognition from point clouds generated through a millimeter-wave radar. In Proceedings of the 3rd ACM Workshop on Millimeter-wave Networks and Sensing Systems. 51-56.
- [45] Ronnie Smith, Yuan Ding, George Goussetis, and Mauro Dragone. 2020. A COTS (UHF) RFID floor for device-free ambient assisted living monitoring. In International Symposium on Ambient Intelligence. Springer, 127-136.
- [46] Wei Wang, Alex X Liu, Muhammad Shahzad, Kang Ling, and Sanglu Lu. 2015. Understanding and modeling of WiFi signal based human activity recognition. ACM MobiCom (2015).
- [47] Gary M Weiss. 2019. Wisdm smartphone and smartwatch activity and biometrics dataset. UCI Machine Learning Repository: WISDM Smartphone and Smartwatch Activity and Biometrics Dataset Data Set 7, 133190-133202 (2019), 5.
- [48] Shigeng Zhang, Zijing Ma, Chengwei Yang, Xiaoyan Kui, Xuan Liu, Weiping Wang, Jianxin Wang, and Song Guo. 2022. Real-time and accurate gesture recognition with commercial rfid devices. IEEE Transactions on Mobile Computing 22, 12 (2022), 7327-7342.